University of Venda

STUDIES ON STRUCTURAL, ELECTRONIC AND OPTICAL PROPERTIES OF SnO_2 DOPED WITH NITROGEN, CHLORINE, ANTIMONY, AND INDIUM

Nekhwevha Nditsheni

(11610687)

Dissertation Presented in Fulfilment of The Requirements for the degree of Master of Science (M.Sc.)

in

PHYSICS

FACULTY OF SCIENCE, ENGINEERING AND AGRICULTURE

UNIVERSITY OF VENDA

SUPERVISOR: PROF N.E. MALUTA (UNIVEN)

CO-SUPERVISOR: PROF R.R. MAPHANGA (CSIR)

YEAR: 2023

Declaration

I, Nekhwevha Nditsheni, declare this dissertation entitled "**Studies on structural, electronic and optical properties of SnO_2 doped with nitrogen, chlorine, antimony and indium**" being submitted for the Masters of Science degree in Physics at the University of Venda has not been previously submitted for a degree at this or any other university. I further declare that this is my work in design and execution and that all referenced material contained therein have been duly acknowledged.

Signed by __  _ at__Thohoyandou_ on the _15_ day of September____2023.

Dedication

This dissertation is dedicated to the Almighty God of Mount Zion and my family.

Acknowledgments

This journey was truly a life-changing experience for me. It would not have been possible for me to achieve it alone without the support and guidance that I have received from many people. Primarily, I would like to thank my supervisor, Prof. N. E. Maluta, for his unwavering support and confidence in me during the entirety of this project. Without your advice and constant feedback, I believe my master's journey would not have been so smooth. It was a great experience to be working with you. I would also like to express my deepest thanks to my co-supervisor Prof R. R Maphanga. I am most grateful for your precious time in guiding and helping me. Many thanks to Mr L. Phuthu for the valuable advice accorded especially towards the end of my research.

To my friends, Ranwaha Tshifhiwa, Thokhozani Mlothswa, Mabaso Vusi, Ratshilumela Dima, Ronella Randela , not forgetting Mr TT Khedzi in the laboratory, I am grateful for having you. Without having all of you, the working atmosphere would not be an enjoyable and cheerful one for me. Thanks for all the help, support, and jokes from you to relieve my stress especially when the road was bumpy. I would like to acknowledge the University of Venda and the Department of Physics for granting me the opportunity to continue with my studies. Finally, I would like to acknowledge financial support from the National Research Foundation (NRF) and the National Institute for Theoretical and Computational Sciences (NITheCs).

Abstract

SnO_2 has recently attracted a great deal of interest due to its many technological applications, including in solar cells as it possesses advantageous optical and electrical characteristics, outstanding chemical stability, and thermal stability. However, the photocatalytic activity and charge carrier mobility are constrained by the large band gap. A cost-effective and efficient method for reducing the SnO_2 band gap and increasing the potential for photocatalytic applications is doping with different elements. Examining how mono-doping and co-doping impact the electronic, structural, electrical, and optical characteristics of the SnO_2 supercell structure, the current theoretical study used Density Functional Theory (DFT) calculations of different metal and nonmetals (N, Cl, In, and Sb) and (N-Cl and In-Sb) as dopants and co-dopants, respectively. The results show that due to the band gap narrowing and the existence of impurity levels in the band gap, all mono-doped and co-doped SnO_2 exhibit some small redshift. The results of the trials and the calculated optical characteristics, such as the dielectric function, reflectivity, absorption coefficient, and energy-loss spectrum, are in good agreement. According to the predicted absorption coefficient, doped SnO_2 has a noticeable band of absorption. Doped SnO_2 exhibits superior absorption in the visible area of the electromagnetic spectrum than undoped, In-doped, Sb-doped, and In-Sb co-doped SnO_2.

Keywords: SnO_2 supercell, Density Functional Theory, Doping, Co-doping Electronic, Optical properties.

Table of Contents

LIST OF FIGURES

Table of figures

LIST OF ABBREVIATIONS

AFM	- Atomic Force Microscopy
CASTEP	- Cambridge Sequential Total Energy Package
Cl	- Chlorine
CB	- Conduction Band
CBM	- Conduction Band Minimum
DFT	- Density Functional Theory
DOS	- Density Of State
DSSC	- Dye Sensitized Solar Cell
DFT +U	- Density Functional Theory Including Hubbard Term
eV	- Electron Volt
EC	- Electrochromic
EDAX	- Energy dispersive X-ray
EIS	- Electrochemical Impedance Spectroscopy
ELF	- Energy Loss Function
EOP	- Electrochemical Oxidation Process
HOMO	- Highest Occupied Molecular Orbital
IEL	- Ionising Energy Loss
I_{PH}	- Photocurrent Density in Short Circuit
IR	- Infrared
In	- Indium

J_{SC}	- Current Density
F	- Fluorine
FF	- Fill Factor
FESEM	- Field Emission Scanning Electron Microscopy
GGA	- Generalised Gradient Approximation
HSE	- Heyd–Scuseria–Ernzerhof
LDA	- Local Density Approximation
LED	- Light Emission Diode
LUMO	- Lowest Unoccupied Molecular Orbital
PDOS	- Partial Density Of State
PBE	- Perdew-Burke Ezernhof
PH	- Planner Heterogeneous
PV	- Photovoltaic
PL	- Photoluminescence
MBE	- Molecular Beam Epitaxy
MB	- methylene blue
MHS	- Multi-Layered Hollow Sphere
Mn	- Molybdenum
NP	- Nanoparticles
NCs	- Nanocrystals
NGNS	- Nitrogen-Doped Graphene Nanosheets
NNWs	- Nanowires

Na	- Sodium
Ni	- Nickel
Sr	- Strontium
Sb	- Antimony
SnO_2	- Tin Dioxide
TiO_2	- Titanium Dioxide
TEM	- Transmission Electron Microscopy
UV	- Ultraviolet
VB	- Valence Band
V_{OC}	- Open Circuit Voltage
Wt	- weight
XRD	- X-ray diffraction
XC	- Exchange Correlation
Zr	- Zirconium

1 CHAPTER ONE

In this chapter, we briefly introduced the energy crisis, implementation of comprehensive strategies and embracing renewable and efficient energy solutions.

1.1 Introduction

There has been a growing demand for energy in the past two decades worldwide. The problems of scarcity of energy, environmental pollution and ozone layer depletion are associated with the use of conventional energy sources such as fossil fuels. Oil has the biggest share of all energy sources (32.9%), followed by coal (30.1%) in the energy mix matrix. The requirement for energy resources to conduct residential and economic activities has increased due to high levels of pollution and the exponential growth of economies [1]. Fossil fuels will eventually run out if we keep using them without switching to sustainable energy sources. Fossil fuel use increases CO_2 emissions, which directly cause climate change and the greenhouse effect. The world's sustainability is thought to be threatened by the greenhouse effect and global warming. Additionally, these issues and the scarcity of fossil fuels encourage the global community to change the energy strategy to include alternate energy sources [2]. Energy policies have been modified to take renewable energy into account as the new source of sustainable energy in order to meet the world's expanding energy demand.

The ideal strategy for resolving the global energy dilemma will be to substitute ecologically benign renewable energy sources for polluting fossil fuels. The future generation of energy sources is expected to include a variety of sustainable energy sources like hydrogen, wind, geothermal, tidal, and solar energy. Solar energy is the greatest contender among these energy sources because it contributes significantly to global electricity generation and accounts for roughly 0.7% of all electricity generation [3]. A current concern is how to transform solar energy into usable energy.

Solar research strives to produce a cost-effective sustainable energy source by improving the conversion efficiency at low cost [4]. An appealing tactic for this is to use Dye Sensitized Solar Cell (DSSC), which are more affordable and environmentally friendly. Given the quantity and diversity of natural dyes, it is crucial to fully comprehend their electrical structure and

energy levels in order to assess their potential for performing light harvesting and sensitizing functions in DSSC. Due to their poor light-harvesting capabilities, DSSC based on dye and semiconductor have a high solar to electric power conversion efficiency that is already exceeding 11% [5]. To improve their efficiency, the doping mechanism of metal and non-metal has been proposed as a resourceful approach [1-6].

DSSC have some distinct advantages over silicon solar cells, such as simple fabrication processes, low manufacturing costs, and compatibility with flexible substrates. The engineering and production of devices that may satisfy the requirements of the photovoltaic cells market for a variety of applications has received a large amount of research attention.

In this study, we investigated the effects of doping SnO_2 with several dopants, including N, Cl, Sb, and In. Using Density Functional Theory (DFT), this work explores the structural, electrical, and optical characteristics of doped SnO_2. The mechanisms of photocatalytic reaction are affected by doping. This research has the potential to advance our understanding of ongoing efforts to create modified semiconductor photocatalysts that are effective in visible light. The objectives of the study were to:

- Calculate structural properties of the system by geometrically optimizing the SnO_2 structure.
- Perform calculation of the electronic properties for the undoped and doped structures of SnO_2.
- Calculate optical properties for the SnO_2 system, i.e., absorption, reflectivity, energy loss function and dielectric function.

Outline of the thesis

There are five chapters that make up this thesis:

1. Chapter one is introduction that includes some background information, problem statement and the purpose of the study.

2. The literature review is presented in Chapter two, and it is broken down into five main sections. Description of DSSC, Electronic properties, band gap engineering, doping and efficiency of DSSC are covered in this section.
3. The computational methods are discussed in Chapter three, with the Density Functional Theory serving as the primary point of emphasis. Also ,the computational software: Biovia Material Studio and Cambridge Sequential Total Energy Package (CASTEP), are discussed in Chapter three.
4. Chapter four present the details of results and discussion in full.
5. Chapter five is the conclusion and summary of all the work done in the whole thesis.

2 CHAPTER TWO

In this chapter, we discussed what has been reported this far about our compounds of interest with existing literature (information) gaps and the fundamental techniques such as band engineering via doping and outline the working principle of dye sensitized solar cells (DSSC) and shortly discuss the primary components of a DSSC. Additionally, we provided the application of SnO_2 in DSSC, factors affecting its light conversion efficiency and mention the main aims of our current study.

2.1 Literature review.

2.1.1 Dye sensitized solar cells.

DSSC have garnered attention for their potential in various applications due to their unique advantages over traditional silicon-based solar cell. DSSC are lightweight and flexible, making them suitable for powering portable electronics such as smartphones, wearable devices, and electronic gadgets. Their flexibility allows integration into various form factors, enhancing the versatility of these device [6]. The DSSC are made up of five primary parts, which are as follows:

1. A transparent conducting oxide (TCO) coated on a glass.
2. A mesoporous oxide layer (typically TiO_2) deposited on the anode to activate electronic conduction.
3. A monolayer of dye bonded on the surface of mesoporous oxide layer to enhance light absorption.
4. Redox-active liquid electrolyte usually the iodide/tri-iodide couple(I^-/I_3^-)

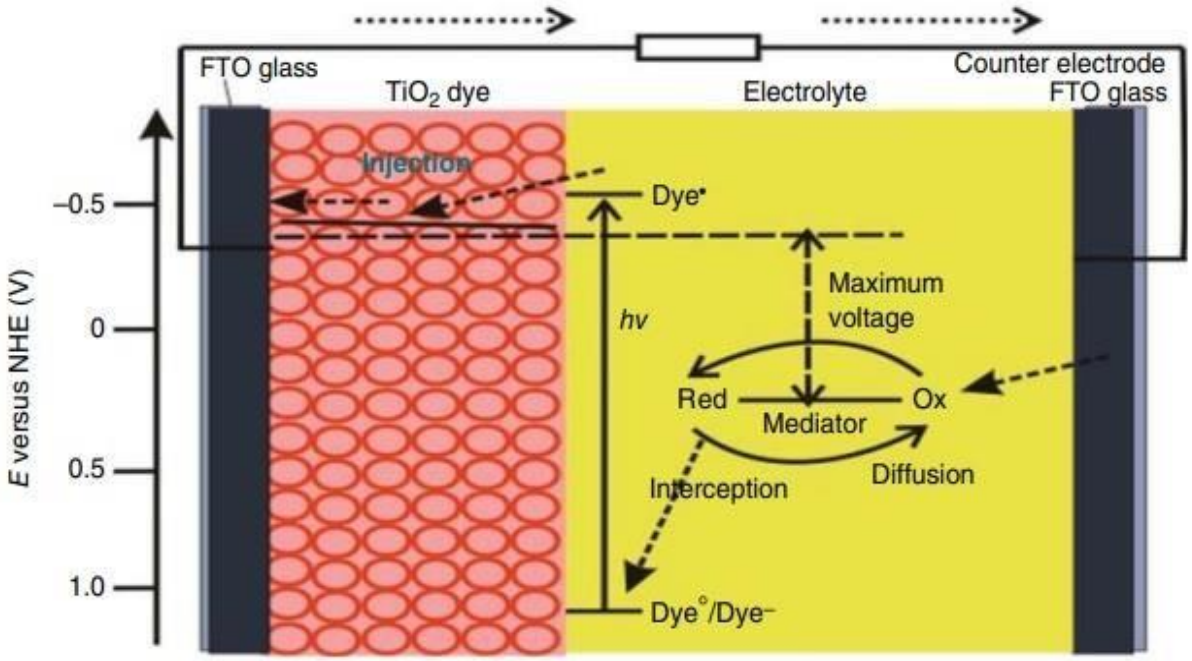

Figure 1: Schematic illustration of the DSSC's operating system [6].

The working principle presented in Figure 1 work as follows:

First, the sun's light is absorbed by the dye molecules absorbed on the semiconductor photo-anode. To create an electric current, excited electrons are introduced into the conduction band (CB) of the semiconductor. The transparent conductive substrate of the counter electrode then receives the electrical current after it has passed through the external wire. The redox mechanism in the electrolyte solution restores the oxidized dye.

In the underneath sub-sections, we briefly discuss the primary constituents of a DSSC.

2.1.1.1 Dye sensitizer.

A dye sensitizer is a key component of DSSC. It plays a critical role in the photovoltaic conversion process by absorbing sunlight and generating excited electrons. Its primary function is to absorb photons from sunlight and convert their energy into electrical energy. When a dye molecule absorbs a photon, it becomes excited, and an electron is promoted to a higher energy level [7]. Dye sensitizers are carefully selected based on their absorption spectra to match the solar spectrum, maximizing light absorption and the efficiency of the DSSC. Dyes with broad absorption spectra and high molar extinction coefficients are

preferred. It also consists of a light-absorbing chromophore, such as a porphyrin or metal complex, attached to a molecular anchor group and a linker moiety. The anchor group attaches the dye to the semiconductor surface, while the linker ensures efficient electron injection into the semiconductor. After absorbing a photon and becoming excited, the dye molecule transfers its excited electron to the conduction band of the semiconductor material (e.g., Tin dioxide, SnO_2) through a process called electron injection. This injection process is facilitated by the favourable energy level alignment between the excited state of the dye and the conduction band of the semiconductor. After injecting its excited electron into the semiconductor, the dye molecule becomes oxidized. It needs to be regenerated by accepting electrons from the redox couple in the electrolyte. This regeneration step completes the electron transfer cycle and allows the dye sensitizer to continue absorbing photons and generating excited electrons [8].

Dye sensitizers are chosen based on various factors, including their absorption properties, stability, ease of synthesis, and compatibility with the electrolyte and semiconductor materials. Each type of dye offers unique advantages and challenges, and ongoing research aims to discover new sensitizers with enhanced performance.

Overall, the choice of dye sensitizer significantly influences the efficiency and performance of DSSCs, making it a critical component in the development of next-generation solar cell technologies.

2.1.1.2 Semiconductor.

A semiconductor is a type of material that has electrical conductivity between that of a conductor and an insulator. These are fundamental to modern electronics and are used in a wide range of electronic devices, including transistors, diodes, solar cells, and integrated circuits. The electronic band structure of semiconductors is characterized by a valence band and a conduction band separated by a band gap. The valence band is occupied by electrons at low energy levels, while the conduction band is empty in the absence of external energy. The band gap is the energy difference between the valence and conduction bands and determines the conductivity of the material [9]. Semiconductors have intermediate conductivity compared to conductors and insulators. At low temperatures, they behave like

insulators because most electrons are bound in covalent bonds. However, as temperature increases, electrons gain enough energy to jump to the conduction band, resulting in increased conductivity. Semiconductors exhibit interesting optical properties, including absorption, emission, and bandgap-related phenomena such as photoluminescence and electroluminescence. These properties make semiconductors valuable in application of DSSC. Wide band gap metal oxide, a semiconductor, is the perfect material for a DSSC photoelectrode because it generates a significant surface cross-sectional area for the anchoring light harvester. Strong surface area, good structural arrangement, strong electron transport, chemical stability, low cost, and environmental friendliness should be the primary characteristics of semiconductors [10].

To speed up charge transport and avoid recombination, a semiconductor has its morphologies, porosity, and layer thickness altered. In the last several decades, there has also been a lot of activity in the area of interfacial electron transport between semiconductor nanoparticles and molecular adsorbates [8].

2.1.1.3 A counter electrode regenerates the redox system.

The counter electrode is typically made of a conductive material, such as platinum (Pt) or a conductive carbon material, to facilitate the electrochemical reactions involved in the regeneration of the redox system. It acts as a catalyst for the reduction reaction, enabling efficient electron transfer kinetics and ensuring the continuous operation of the DSSC [6].

The counter electrode in DSSC catalyses the reduction of triiodide ions in the electrolyte. Optimizing the counter electrode material and structure can enhance electron transfer kinetics and improve overall device performance. The overall device architecture, including the arrangement of components and interfaces, affects the efficiency of charge collection and extraction.

2.1.2 Application of DSSC.

DSSC can be integrated into building materials such as windows, façades, or roofing tiles, enabling the generation of electricity without compromising the aesthetics of the building. This application is particularly attractive for green buildings and sustainable architecture. It can also be used in remote or off-grid areas where access to conventional power sources is

limited, DSSC can provide an alternative solution for electricity generation. These cells can be deployed in rural areas, disaster-stricken regions, or in outdoor signage and lighting systems. This is also applicable in military applications such as powering remote surveillance equipment, communication devices, and portable power packs for soldiers in the field. Their lightweight and portable nature make them advantageous in such scenarios. DSSC can be integrated into the body panels or windows of vehicles to harness solar energy for auxiliary power, reducing the load on the vehicle's primary electrical system and improving fuel efficiency in hybrid or electric vehicles. These applications demonstrate the versatility and potential of dye-sensitized solar cells across various industries and fields, contributing to the advancement of renewable energy technologies and sustainable development.

2.1.3 Factors affecting conversion efficiency of DSSC.

The conversion efficiency of DSSC is a crucial parameter that measures how effectively they convert incident sunlight into electrical energy. DSSC utilize a photosensitive dye to absorb sunlight. The efficiency of light absorption depends on the spectral response of the dye and its coverage over the surface area of the electrode. After absorbing photons, the dye molecules generate electron-hole pairs. Efficient charge separation and transport mechanisms are essential to prevent recombination of these charges, which can reduce overall efficiency. This process heavily relies on the design of the electrode materials and the electrolyte. The electrode structure, typically consisting of a porous layer of nanoparticles coated with the dye, plays a significant role in facilitating efficient charge transport and maximizing the surface area available for light absorption. The electrolyte in DSSCs serves as a medium for ion transport and also affects charge recombination rates. Different types of electrolytes, such as liquid, solid-state, or quasi-solid-state, can impact the device's efficiency. The choice of dye sensitizer greatly influences the spectral response and efficiency of the DSSC [11].

The current state-of-the-art DSSC achieve conversion efficiencies of over 14–15% in laboratory settings. However, commercial DSSC typically have lower efficiencies, often around 10%, due to factors such as stability, absorptivity, and scalability [12]. Ongoing research aims to improve the efficiency and stability of DSSC for practical applications in

renewable energy generation By considering the following formula, one may comprehend the effectiveness of the DSSC:

$$\eta = FF\frac{VV_{OC}J_{SC}}{P_{in}} \quad \text{..... (1)}$$

It provides solar cells' power conversion efficiency. Here, *FF* stands for fill factor, J_{sc} for short circuit current, V_{oc} for solar cell open circuit voltage, and P_{in} for incident light power, which is calculated as brightness times cell area. It is well known that while J_{sc} is inversely proportional to the band gap, V_{oc} is proportional to the band gap. The Shockley-Quessier asserts that reducing a band gap of 1.5 eV results in improved efficiency. It would be preferable to minimize the band gap, which is 3.6 eV [7].

Four parameters determine the total conversion efficiency of a DSSC: the intensity of the incident light (I_s), the photocurrent density at short circuit (I_{ph}), the open circuit voltage (V_{oc}), and the fill factor (*ff*). Therefore, to improve efficiency, the product of V_{oc} and I_{ph} should be optimized. In a photovoltaic device, the photoanode is perhaps one of the most important components, which directly determines the photocurrent, V_{oc}, and cycling performance of the cell, hence materials now are mainly composed of SnO_2 due to its good stability against photo-corrosion and excellent electronic properties. Since some of the materials have drawbacks, such as electron recombination and slow electron diffusion, SnO_2 can be used as an alternative semiconductor to TiO_2 due to its advantages [7]. To obtain higher efficiency, considerable effort has been made to tune the morphology of SnO_2 and cause electron migration from the VB to the CB, since this also affects the optical absorption of the DSSC.

Lachhab *et al*. focused on how the properties of the SnO_2 structure are affected by the layer to improve performance. They obtained a fill factor of roughly 85.56% and an efficiency of 31.41% measured at 1.37 V for the short circuit voltage and 25.86 mA/cm^2 for the short circuit current density, their analysis showed a considerable improvement in the structure's performance. A comparison with measurements taken on the same structure, which reveals an increase of 6.62% based on the components that were detected, validates these findings [8].

According to Basu *et al*. SnO_2 particles with an average size of 20 nm were used in the creation and testing of DSSC. They discovered that the modification improved the open-circuit voltage, fill factor, and short circuit current, resulting in an almost two-fold increase in power conversion efficiency, from 1.48% with no treatment to 2.85% with $TiCl_4$ treatment. According to electrochemical impedance spectroscopy (EIS) performed in the dark, the longer electron lifespan and decrease in recombination of electron to the electrolyte are what cause the greater photovoltaic performance of the DSSCs. Their research shows that titania modification of the SnO_2 and FTO anodes can greatly boost photo conversion efficiency [10].

Since the DSSC needs a large surface area for light collection and a densely packed microstructure for faster electron transport. Instead of focusing only on the surface area of the material, it is best to examine how the atoms are arranged within the structure [9].

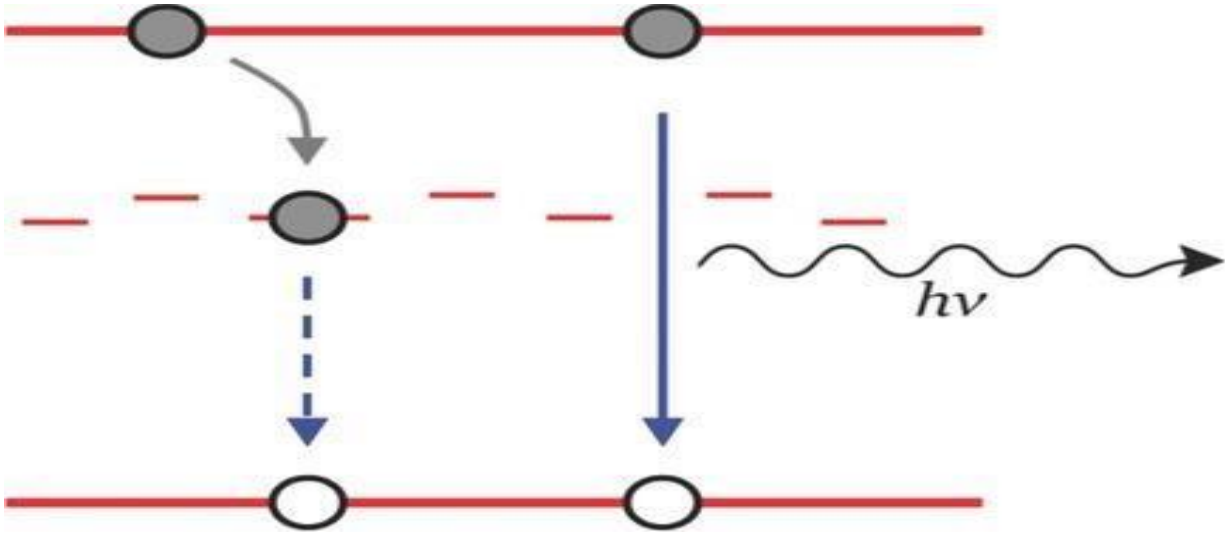

Figure 2: Depiction of electron recombination [12].

In solid-state physics of semiconductors, charge recombination is the process by which mobile charge carriers are created and eliminated. The charge recombination process is fundamental to the operation of many optoelectronic semiconductor devices such light emitting diodes (LED) and DSSC. Most studies presented theoretical work to comprehend and suppress charge recombination, using first principles-based approaches within the context of time-dependent DFT (TD-DFT) for metal-free organic dyes [12-13].

Based on the results of the charge recombination kinetics calculations of 2020 by Samantha *et al*. the addition of a thiophene unit between the acceptor unit and the bridge effectively slows down the recombination process. The investigation revealed that, using anticipated electron injection and hopping durations, the key factors affecting the performance of the DSSC device exhibit a linear connection with computed cold electron injection efficiency [13]. Subsequently, the combined approach using rate theory applications and electronic structure calculations could assist in the design of efficient DSSC sensitizers by optimizing photo-induced charge transfer and energy transfer processes.

2.1.4 SnO_2 semiconductor.

SnO_2 is a semiconductor with a wide band gap [10]. Its outstanding chemical and thermal stability, exceptional optical and electrical qualities, and other characteristics all contribute to this. TiO_2's Isostructural rutile phase is more frequently utilized in DSSC as a semiconductor than SnO_2's rutile phase, which is thermodynamically stable and advantageous for solar cell applications [14].

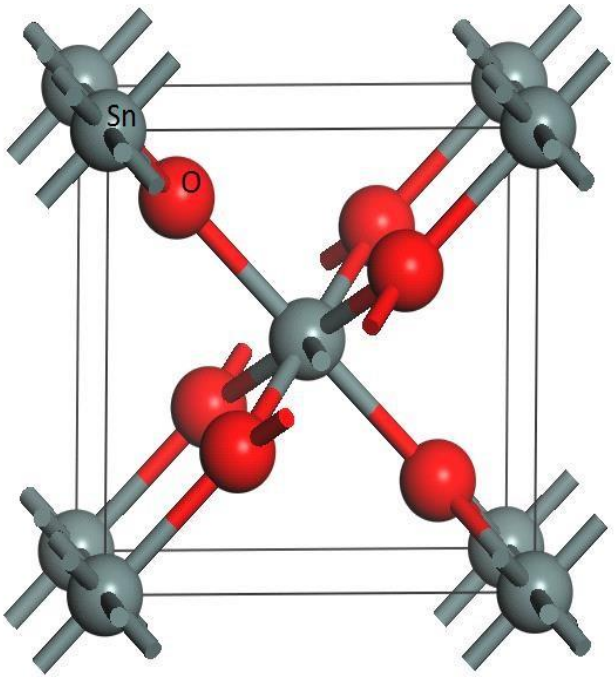

Figure 3: SnO_2 crystal structure.

SnO_2 has at least two advantages over other semiconductors applied in DSSC, i.e., it has higher electron mobility (~100-200 $cm^{-2}V^{-1}s^{-1}$) and faster diffusion transport of photoinduced

electron as reported by Tran *et al*. [15,17]. Additionally, it enables incredibly efficient electron injections from the absorbed dye molecule. Due to these advantages, it is frequently used in numerous applications, such as DSSC and other applications [18]. An effective photo-anode for DSSC should have characteristics like high dye molecule loading, advantageous band alignments, and good electron transport efficiency. As described by Ma *et al*. they further confirmed that the high charge mobility of SnO_2 accelerated the transport of electrons and that the highly crystalline NCs prevented photo-electron recombination. Due to the impacts of quantum size, CBM of the SnO_2 NCs was elevated [18]. Consequently, its wider band gap of 3.6 eV, which results in fewer oxidation holes in the valence band (VB), the DSSC's extended stability is made possible. Furthermore, even though SnO_2 has a lower fill factor, its employment in DSSC has a significant impact on the current density (J_{sc}) value and photo-conversion efficiency.

2.1.5 Band gap engineering.

Band gap engineering refers to the deliberate manipulation of the electronic band gap in semiconductor materials to tailor their optical and electrical properties for specific applications. This concept is widely used in semiconductor device design, including solar cells, light-emitting diodes (LEDs), and transistors. Introducing impurities into the semiconductor crystal lattice to modify its electronic properties. Doping can be used to shift the Fermi level, alter the band structure, and change the band gap of the material. Forecasting the photo-physical and photochemical properties of semiconductors requires an accurate estimation of the band gap energy.

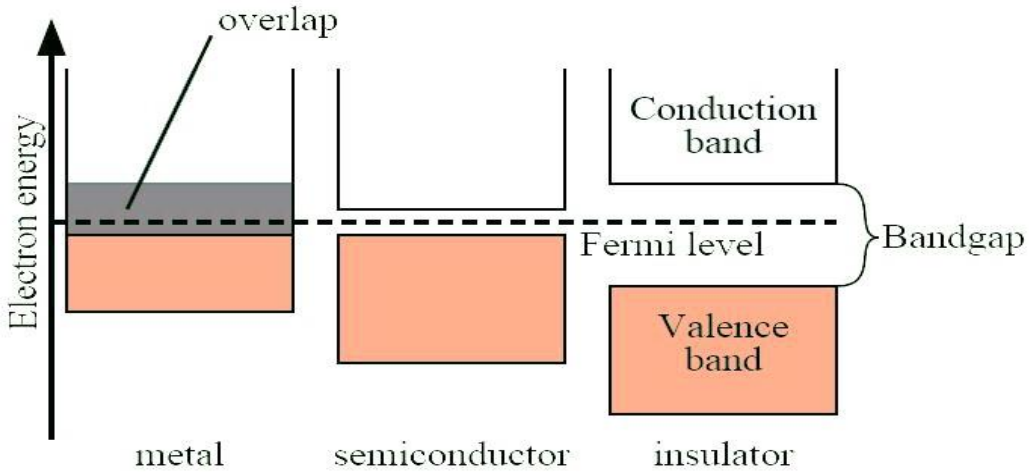

Figure 4: Energy difference between the CB and the top of the VB [12].

Li *et al*. used both the augmented spherical wave supercell band structure approach and the self-consistent scatter wave molecular orbital cluster approach to compute the electronic structure and related parameters of Sb doped SnO_2. A semiconducting behaviour with a relaxation process moved to higher frequencies, typical of the doping mechanism of charge carriers, was discovered to be indicated by the thermal change of electrical conductivity [19]. It was further stated that the main drawback was caused by the SnO_2 conduction band edge's 300 mV positive shift, which causes fast electron recombination. This is illustrated in Figure 3 where the grey circles represent electrons, and the white circles represent electrons. According to Dissanayake *et al*., the fastback-electron transfer rate of SnO_2 is due to the material's low conduction band edge value, which speeds up electron recombination and reduces electron trapping density [12].

Consequently, the low wavelength threshold encompasses practically the whole solar spectrum that reaches the Earth's surface, the optimal band gap has been variably estimated to range from about 1.0 eV up to about 1.5 eV (depending on various assumptions). Wide band gap photovoltaics are a crucial component for collecting the portion of the spectrum beyond the infrared. Creating DSSC that more efficiently gathers light from diverse spectrum regions is a key area of research in solar energy. The larger band gap of SnO_2 (3.6 eV)

compared to anatase TiO_2 (3.2 eV) is advantageous since it would lead to a reduction of oxidative holes in the valence band, assisting in the prolonged stability of DSSC.

Pazouki *et al*. used a hydrothermal method and SnO_2 nanostructures were produced. It was stated that the samples' band gaps, at standard temperature, were about 3.46 eV, which is less than the band gap of pure tin oxide. However, the bulk band gap of the material and the samples produced at higher temperatures were identical. This suggests that the ultrafine SnO_2 nanoparticles exhibited a band gap contraction [20].

Sol-gel production of nickel-doped tin oxide nanoparticles (sub-5 nm size) with strong fluorescence emission characteristics was demonstrated by Lin *et al*. The structural and compositional study has been conducted using XRD, TEM, FESEM, and EDAX. The band gap narrowing effect is visible in the optical absorbance spectra, and it was shown to become more pronounced as nickel content increased. The SnO_2 alloying effect can be attributed to the band gap shrinking; however, at higher doping levels, it may result from the creation of defect sub-bands below the conduction band [21].

Zhou *et al*. fully explored experimentally and theoretically the impact of mismatched stress on the structural, electrical, and optical properties of SnO_2 thin epitaxial films. They found that when the thickness of the epitaxial sample increases, the tensile strain in thin films decreases. While the tensile strain increases at the BC location, the optical band gap substantially contracts. To change the band gap of SnO_2, biaxial strain is preferred to uniaxial strain [22].

2.1.6 Dopants.

A dopant, also known as a doping agent, is a small amount of an impurity element that is added to a chemical substance to change the chemical material's original electrical or optical properties. A very small amount of dopant is normally required to produce changes. The dopant atoms are integrated into the crystal lattice of the crystalline substance when doped. The choice of an optical species as a dopant in semiconductors is influenced by a few important parameters, such as the understanding of the activation limit and the diffusivity dependent on the dopant incorporation method [23]. The material's bond strength is one of the major factors in choosing an atom since it affects implant tools and the temperature-

dependent amorphization threshold. Furthermore, the structure of the tin oxide may be altered because of bond length disorder.

The most persuasive proof that Group 4 doping can be employed as n and p type dopants comes from experiments using Molecular Beam Epitaxy (MBE) [24]. Common dopants used in this work include Nitrogen (N), Chlorine (Cl), Indium (In) and Antimony (Sb). In semiconductors, charge carriers are electrons and holes. Electrons are negatively charged and move in the conduction band, while holes, which represent the absence of electrons in the valence band, behave as positively charged carriers. The mobility of charge carriers determines the material's properties. In this work SnO_2 was doped with different dopants so that defects can be created, and this will alter the electronic properties and charge mobility will also be improved.

2.1.7 Doping of SnO_2

Doping is a process used in semiconductor technology to intentionally introduce impurities into a semiconductor crystal lattice to modify its electrical properties. By adding specific types and concentrations of dopants, semiconductor materials can be tailored for various applications. Doping is primarily used to alter the conductivity, carrier concentration, and other electronic properties of semiconductor materials. It allows engineers to control the behaviour of charge carriers (electrons or holes) within the material, enabling the design of semiconductor devices with desired characteristics. Donor dopants introduce additional free electrons into the semiconductor crystal lattice, thereby increasing the concentration of negative charge carriers (electrons). Common donor dopants include elements from Group V of the periodic table, such as phosphorus (P), arsenic (As), and antimony (Sb). Doping is fundamental to the fabrication of various semiconductor devices, including diodes, transistors, solar cells, and integrated circuits. It enables the design of materials with specific electrical properties tailored for different applications, such as high-speed transistors, low-noise amplifiers, and photodetectors.

Overall, doping plays a crucial role in semiconductor technology, allowing for the precise control and manipulation of semiconductor materials to meet the requirements of modern electronic devices The first use of semiconducting materials and the subsequent

technological advance of manipulating their electrical properties through doping establish the foundation for the vast array of electronic devices that permeate today's information society.

Doping an inorganic semiconductor entail shifting the electronic bands' energy alignment in relation to those of metal contacts and other doped semiconductors. In contrast to the non-metal ions, which are employed as anionic dopants to replace the O anion, metal ions are utilized as cationic dopants to replace the Sn^{4+} cation of SnO_2 [25].

To alter the optical and photo-electrochemical characteristics of metal oxide semiconductors, several metal dopants have been added. According to Afify *et al*. when Sn is replaced with Co^{2+} when doping SnO_2, the lattice cell contracts due to the minor change in the dopant's radius, lowering or contracting the band gap [26]. Another study showed that substitution of Sn with Zr^{4+} atom results in an increased band gap [27]. The findings reported that if the 2p state of oxygen remains unchanged, the shifting band gap is mostly caused by a shift in the conduction band minimum.

A thorough investigation was conducted on how Pb doping on SnO_2 affected how large its band gap was. The findings exhibited that 15% Pb doping significantly reduced the band gap to as low as 0.8 eV (3.64 eV-2.87 eV). According to Zheng *et al*., the band gap tunability seen with Pb addition offers an easy and practical way to successfully tune the band gap and is likely to open potential in the development of oxide opto-electronic and energy applications [28].

According to Filippatos *et al*. structural modifications and their effects on the electrical characteristics of halogen (F, Cl, Br, and I) doped SnO_2 were investigated using DFT simulations. They evaluated how intercalated atoms affected the electrical structure and optical characteristics of the doped SnO_2 at either interstitial or substitutional sites. Each time, gap states were produced, and the band gap value was considerably decreased. These dopants were also employed to make a single acceptor and donor by placing them in the appropriate interstitial and substitutional regions. This may also be seen in the density of state, where gap states would appear right above or right below the valence band, respectively. The optical and electrical properties of SnO_2 could be considerably changed by these gap states [29].

Oshima *et al*. used GGA to analyse the electronic structures of SnO_2 doped with Cl and Sb. First-principles calculations were successful in examining the effects of the dopant in SnO_2. They discovered that the antibonding Sn-5s and O-2p orbitals that make up the CBM of SnO_2 are different from the non-bonding O-2p orbitals that make up the VBM of SnO_2. The calculated results for Cl and Sb doped SnO_2 show that the impurities behave as n-type dopants and exhibit shallow donors' levels in the conduction band [30].

To investigate the structure, surface, and electrical properties of a variety of indium-doped (In-SnO_2) thin films, Bhatia *et al*. adopted the spray-pyrolysis method. On the characteristics of SnO_2, the impacts of indium filler content (between 0 and 15 weight percent) have been investigated. According to structural analysis, the integration of indium after a particular optimal value leads in structural deformation, which causes the film to expand in the c-axis direction. The ideal value for transitioning from n- to p-type is revealed in the electrical study extract, and more evidence is provided by Hall measurement. The most effective transition from n-type to p-type conductivity is known to occur at a 6 wt% shift. It has been demonstrated that this mechanism is best suited for the low temperature range [31].

Duan *et al*. effectively altered nitrogen-doped graphene nanosheets (NGNS) electrode using the dip coating and sol-gel processes. Comparing the NGNS-modified electrode to other electrodes, they find that it has a smaller unite crystalline volume (71.11 vs. 71.32), lower charge transfer resistance (10.91 vs. 21.01), and lower electrical resistivity (13 m vs. 34 m). The accelerated lifetime of the electrode is 4.45 times greater than that of the pure SnO_2 electrode. They demonstrate that the electrocatalytic efficiency can be increased by adding NGNS to the active coating by voltametric charge analysis and Xray photoelectron spectroscopy tests [32].

Filippatos *et al*. published theoretical DFT-based research that examines the impact of doping on SnO_2, mainly at substitutional positions 16–24, in addition to their experimental work. The band gap was shown to be the location of single donor states, notably for halogen substitutional doping; nonetheless, the community typically disregards the effect of interstitials [33].

DFT were utilized to assess the results of Carbon and Nitrogen doping on the band edges doped VO_2, according to Wang *et al*. They discovered that the band gaps of N-doped VO_2 were lower than those of pure VO_2 which is 0.78 eV. Since the C-doped VO_2 had the smallest band gap (0.43 eV), it may be assumed that this material has the greatest potential for developing effective thermochromic energy-saving properties. These findings will make it possible to create a novel method of regulating the VO_2 phase transition [34].

Iwakura *et al*. examined the chemical and physical aspects of anodic development for oxygen and chlorine on SnO_2 film electrodes doped with foreign metals. Electrodes doped with noble metals often exhibit much superior anodic characteristics compared to electrodes doped with base metals. Every characteristic of the noble metal doped electrodes was replicated in the oxygen evolution process, which served as the reaction's active core. It was shown that the kind of noble metals doped in such electrodes has no effect on the chlorine evolution reaction, and a plausible mechanism for this reaction was proposed that involves the overflow of Cl radical from noble metal to Sn sites hence it will be doped on the O site [35].

Deyu *et al* produced pure and SnO_2 coatings doped with chlorine using the spray pyrolysis method. It was examined and compared to the effects of other types of doping to see how chlorine doping affects the electrical and optical properties of SnO_2. The allowed direct and indirect transitions are considered throughout the analysis and interpretation of the absorption coefficient data vs. photon energy. The figure of merit is highest, and the electrical resistance is minimal for SnO_2 doped with 0.4 wt% Cl [36].

On silica glass substrates, Wang *et al*. created pure and Sb-SnO_2 using a chemical spray approach. The produced films were characterized using X-ray diffraction (XRD), atomic force microscopy (AFM), ultraviolet-visible spectroscopy studies. According to the XRD data, all films had a tetragonal cassiterite SnO_2 structure. The Sb inclusion in the cassiterite lattice decreased the transparency in this region, which was greater than 70% in the Sb-doped films. An electrochemical photocurrent test revealed that a 4% doping level resulted in the highest rising current under UV light [37].

Boomashri *et al*. presented Sb doping's effects on the gas-sensing system of SnO_2 thin films made by utilizing a nebulizer-assisted spray pyrolysis technique. Fundamental properties of

the transparent conducting oxide were found to be improved after 0 to 5 wt% Sb-doping. At room temperature, ammonia concentrations between 50 and 250 ppm could be detected using the deposited films. The characteristics of the Sb-doped SnO_2 films were analysed using a variety of analytical techniques. In particular, a significant grain size was seen in the morphological pictures, which exhibited spherical grains in pure SnO_2 films and their change to a trigonal structure after Sb doping [38].

Despite the high electrochemical activity of antimony doped tin oxide (Sb-SnO_2) based electrodes, stability is still a significant issue, claim Zhang *et al*. [39]. Therefore, it is vitally necessary to develop techniques for preventing electrode materials from becoming inactive during the electrochemical oxidation process (EOP). They provided information on a workable technique for prolonging electrode lifetime without lowering electrochemical activity.

This research focused on analysing the structural, electronic and optical properties of SnO_2 doped with N, Cl, Sb. The characteristics of this doped SnO_2 for usage in DSSC have not received much attention. Understanding the theoretical component is crucial to improving the experimental investigation of the subject.

3 CHAPTER THREE

Here, we provided the theoretical framework from which this study was based on, starting from the Schrödinger equation and Density Functional Theory formalisms all the way to basic computational simulations.

3.1 Theoretical framework

3.1.1 Schrödinger equation

This is a fundamental physics equation that describes a system's quantum mechanical behaviour. It is a partial differential equation that describes how a physical system's wave function evolves over time. The following is the time dependent one-dimensional Schrodinger equation:

$$i\hbar\frac{\partial\Psi(r,t)}{\partial t} = H\Psi(r,t) \quad \text{.....(2)}$$

H is the Hamiltonian operator, which is characterized as:

$$H = \left(\frac{i\hbar^2}{2m}\nabla^2 + V\right) \quad \text{.....(3)}$$

where $\hbar$ is the Planck's constant divided by 2π and m is the mass of the electron, φ is a wave function, r is the position, t is the time whereas ∇^2 is the Laplace operator and V is the potential energy. When the Hamiltonian operates on a wave function, it gives the energy of the wave function.

$$\left(\frac{-\hbar^2}{2m}\nabla^2 + V(r)\right)\Psi(r,k) = E(k)\Psi(r,k) \quad \text{.....(4)}$$

To determine a crystalline solid's band structure, or the energy-momentum $[E(k)]$ connection, the Schrodinger equation of a rough one-electron issue is typically solved [40].

3.1.2 Density Functional Theory

Density Functional Theory (DFT), a computational quantum mechanical modelling method, is used to study the ground-state electron density of many-body systems as well as the electronic structure of atoms and molecules. Using functionals, in this example the spatial-dependent electron density, the DFT can be utilized to ascertain the characteristics of a many-electron system. DFT is computationally versatile and has also been expanded to include

these topics [41]. As a result, DFT is frequently used in first principles computations to describe and predict properties of molecular and condensed matter systems [42].

3.1.3 First principle calculation

A wave function in quantum mechanics describes the quantum state of a set of particles in an isolated system. The ground state for a collection of atoms can be obtained by solving the Schrodinger equation [43].

$$E\Psi_i = H\Psi_i \quad (5)$$

Knowledge from the Born Oppenheimer approximation that indicates that the dynamics of atomic nuclei and electrons can be separated is using,

$$m_{nuclei} \gg m_e \quad (6)$$

where m_{nuclei} is the mass of the nuclei and m_e is the mass of the electron. The nuclei are heavy and slow while the electron is small and fast. The dynamics of nuclei and electrons are decoupled into two wave functions:

$$\Psi_i\{(r_i),(R_I)\} = \Psi_N(R_I) * \Psi_e(r_i) \quad (7)$$

For many-particle problems in the solid state, the Schrodinger equation is solved for electrons in the form:

$$H\Psi_i(r_1, r_2, r_3 \ldots r_N) = E\Psi_i(r_1, r_2, r_3 \ldots r_N) \quad (8)$$

The electron Hamiltonian consists of terms that include electrons, and it has three important terms as presented in equation (9) below:

$$H = -\frac{\hbar^2}{2m_e}\sum_i^{N_e} \nabla_i{}^2 + \sum_i^{N_e} V_{ext}(r_i) + \sum_{i=1}^{N_e}\sum_{j>1}^{Ne} U(r_i, r_j) \quad (9)$$

where the first term is the kinetic energy term, the second term is the potential energy term indicating the electrons interacting with the nuclei and the third term is the electron-electron repulsion term, whereas V_{ext} is the external potential [44].

For the DFT, it is possible to move from the wave functions to electron density. The electron density is defined by the expression:

$$n(r) = \Psi^*(r_1, r_2, r_{3,} \dots r_n)\Psi(r_1, r_2, r_{3,} \dots r_n) \dots\dots\dots\dots\dots\dots\dots\dots\dots\dots\dots (10)$$

Only three dimensions exist in electron density. The many-electron problem is reduced to numerous one-electron difficulties by treating one electron as a point charge in the field of all the other electrons.

$$\Psi\left(r_1, r_2, r_{3,} \dots r_N\right) = \Psi(r_1) * \Psi(r_1) * \Psi(r_1) * \dots \Psi(r_N) \dots\dots\dots\dots\dots\dots (11)$$

Equation (11) is known as the Hartree product.

Now the electron density is defined in terms of the individual electron wave functions as:

$$n(r) = 2\sum_i^N \Psi_i^*(r) * \Psi_i(r) \dots\dots\dots\dots\dots\dots\dots\dots\dots\dots\dots\dots\dots\dots (12)$$

3.1.4 Hohenberg and Kohn theorems

The Kohn-Sham DFT is built on the theorems. The core tenet of DFT is that one may precisely infer from the ground state density both the excited and ground state features of a many-electron system in the presence of an external field. Two fundamental theorems exist [45].

Theorem 1:

The electron density's special functional, $E[n]$, which is given by:

$$E[n] = T[n] + U[n] + \int V(r)n(r)d^3r \dots\dots\dots\dots\dots\dots\dots\dots\dots\dots\dots (13)$$

is the source of the ground state energy [57] :

$$E[n] = E[n(r)] \dots\dots\dots\dots\dots\dots\dots\dots\dots\dots\dots\dots\dots\dots\dots\dots\dots (14)$$

Thus, the electron density is all that is required to define the total ground state energy.

Theorem 2:

The genuine ground state electron density is the one that reduces the overall functional's energy. This theorem reveals how to locate the ground state energy indicated by the following expression:

$$E[n(r)] > E_0[n_0(r)] \dots\dots\dots\dots\dots\dots\dots\dots\dots\dots\dots\dots\dots\dots\dots\dots (15)$$

The energy functionality consists of two main parts, the known and the unknown energy.

$$E[\{\Psi_i\}] = E_{known}[\{\Psi_i\}] + E_{XC}[\{\Psi_i\}] \quad \text{.....(16)}$$

The known energy term is given by:

$$E_{known}[\{\Psi_i\}] = -\frac{\hbar^2}{2m_e}\sum_i^N \int \Psi_i{}^* \nabla^2 \Psi_i d^3r + \int V(r)n(r)d^3r + \frac{e^2}{2}\int \frac{n(r)n(r')}{r-r'} d^3r d^3r' + E_{ion} \quad \text{.....(17)}$$

The unknown energy term $E_{XC}[\{\Psi_i\}]$ is called the exchange correlation functional and it takes care of all the quantum mechanical interactions between electrons. It includes all quantum mechanical terms, and it is not known but needs to be approximated.

3.1.5 Exchange correlation functionals

The single variable that influences the local density approximation, which is based on the local electron density, is density. The exchange-correlation(XC) functional is presumed to be known in the formulation above. Most recent density functional computations use the LDA since numerical XC potentials have now only been established for a small number of straightforward model systems. The LDA reduces the complexity of the XC functional to a straightforward function of density at any location r. The value of this function is the XC energy per electron in an electron density n(r) that is uniform and

homogeneous. The LDA expression for $E_{XC}[n(r)]$ is given by

$$E_{XC}[n(r)] \approx \int E_{XC}\big(n(r)\big)n(r)dr \quad \text{.....(18)}$$

The generalized gradient approximation (GGA) method was created as a result of the fact that the LDA method only considers the electron density n(r) at point r for the purpose of approximating the XC energy; the gradient of the density n(r) is not used in this process. The projected binding and dissociation energies are improved by the GGA, particularly for systems containing hydrogen. Although there are many GGAs, Perdew, Burke, and Ezernhof's (PBE) GGA is one of the most popular [45]. The standard exchange correlation functional is GGA-PBE given by

$$E_{XC}^{PBE} = \frac{1}{4}E_X^{HF} + \frac{3}{4}E_X^{PBE} + E_C^{PBE} \quad \text{.....(19)}$$

Where E_X^{HF} is the Hatree-fock exact exchange functional, is the PBE exchange functional and E_C^{PBE} is the PBE correlation [69].

It is advised, particularly for research on molecules interacting with metal surfaces, however, bulk computations can further be trusted to be accurate. Compared to LDA functionals, the GGA technique provides a better overall description.

3.1.6 The Kohn-Sham Scheme

Kohn and Sham introduced a method based on the Hohenberg-Kohn theorem that enables one to minimize the functional $E[n(r)]$ by varying $n(r)$ overall densities containing N electrons [45]. This constraint is introduced by the Lagrange multiplier μ chosen so that $\int n(r)dr = N$

$$\frac{\delta}{\delta n(r)}[E[n(r)] - \mu \int n(r)dr] = 0 \quad \text{.....(20)}$$

$$\Rightarrow \mu = \frac{\delta E[n(r)]}{\delta n(r)} \quad \text{.....(21)}$$

Kohn and Sham chose to separate $E[n(r)]$ into three parts, so that $E[n(r)]$ becomes:

$$E[n(r)] = T_s[n(r)] + \frac{1}{2}\int \frac{n(r)n(r')}{|r-r'|}drdr' + E_{XC}[n(r)] + \int n(r)V_{ext}(r)dr \quad \text{.....(22)}$$

where $T_s[n(r)]$ is defined as the kinetic energy of a non-interacting electron gas with density $n(r)$ and is given by,

$$T_s[n(r)] = -\frac{1}{2}\sum_{i=1}^{N}\int \Psi_i^*(r)\nabla^2\Psi_i(r)dr \quad \text{.....(23)}$$

Equation (16) also acts as a definition for the exchange-correlation energy functional $E_{XC}[n(r)]$. We can rewrite equation (15) in terms of an effective potential $V_{eff}(r)$ as follows:

$$\frac{\delta T_s[n(r)]}{\delta n(r)} + V_{eff}(r) = \mu \quad \text{.....(24)}$$

where

$$V_{eff}(r) = V_{ext}(r) + \int \frac{n(r')}{|r-r'|}dr' + \frac{\delta E_{XC}[n(r)]}{\delta n(r)} \quad \text{.....(25)}$$

Now, if one considers a system that really contained non-interacting electrons moving in an external potential equal to $V_{eff}(r)$ as defined in equation (24), then the same analysis would lead to the same equation. Therefore, to find the ground state energy and density, E_0 and $n_0(r)$, all one must do is to solve the one electron equations using the relation:

$$\left(-\frac{1}{2}\nabla_i^2 + V_{eff}(r) - E_i\right)\Psi_i(r) = 0 \quad \text{.....(26)}$$

As the electron density is constructed according to the expression:

$$n(r) = \sum_{i=1}^{N}|\Psi_i|^2 \quad \text{.....(27)}$$

These equations must be solved with self-consistency scheme [46].

3.1.7 Self-consistency scheme

The Self-consistency scheme is shown in Figure 4. This scheme determines the electron density, it consist of 4 steps and are summarized as follows:

Step 1: Guess the electron density - trial $n(r)$.

Step 2: Solve the Kohn-Sham equations with $n(r)$, to obtain single electron wave function $\Psi_i(r)$.

Step 3: Calculate the electron density based on the single-electron wave functions given by equation (12):

Step 4. Compare the new electron density $n(r)$ with the initially approximated electron density $n(r)$ from step 1.

There are two conditions to consider before concluding about the electron density, namely:

If the new density is different from the approximated density, begin with the new electron density as the approximated and repeat the whole procedure from step 1.

If they are both the same, then that means true ground state electron density has been obtained.

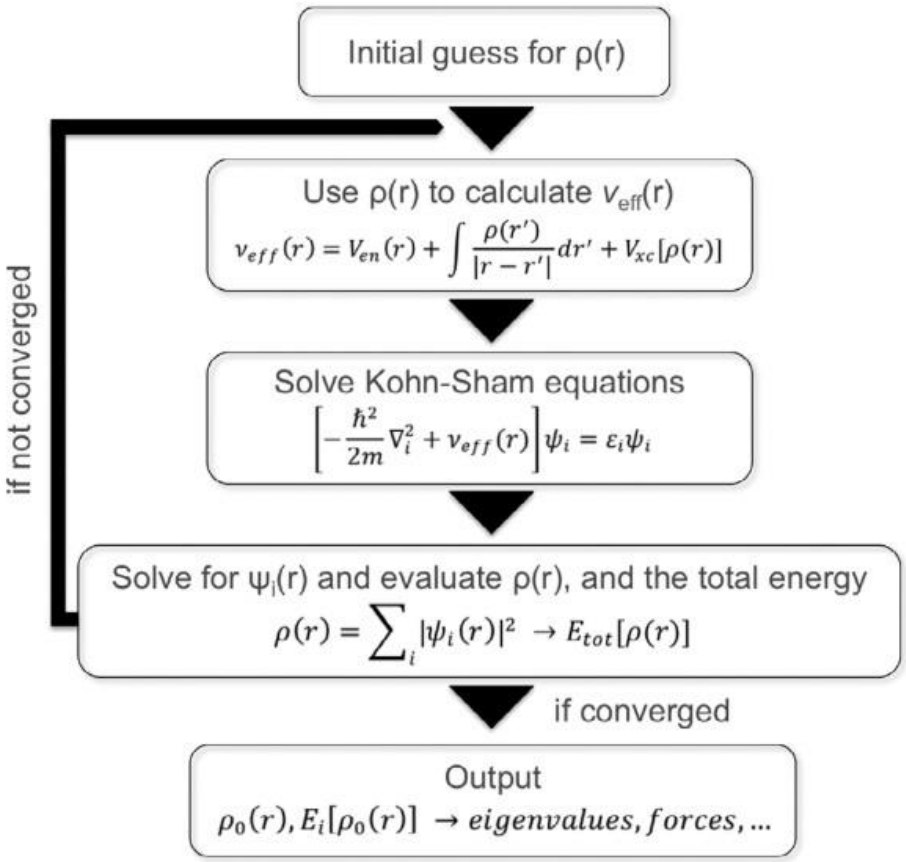

Figure 5: A general self-consistent scheme to solve the Kohn–Sham equation [46].

3.2 Computational software

3.2.1 Material studio

A complete modelling and simulation environment called Material Studio was created to help researchers in various fields forecast and comprehend the connections between a material's atomic and molecular structure and its properties and behaviour. Using material studio, researchers are creating a variety of materials with improved performance . We can use the Density Functional Theory for computations, thanks to the Cambridge Serial Total Energy Package (CASTEP), a feature of the material studio application.

CASTEP provides first-principles calculations of the electrical characteristics of crystalline solids, surfaces, molecules, liquids, and amorphous materials using Density Functional Theory and a plane wave basis set. The only restriction is the restricted speed and memory

of the computers being used, which makes it possible to calculate the properties of any substance that can be conceived of as an assembly of nuclei and electrons.

Common applications include analysing optical properties, band structure, density of states, and surface chemistry. Additionally, CASTEP can be used efficiently to research the properties of both point and extended defects, such as grain boundaries and dislocations, in semiconductors and other materials [47].

3.2.2 Computational simulation

First-principles calculation can help us comprehend the dye or semiconductor contact that is at the core of DSSC better. To enhance performance and reduction of the band gap, we simulated the DSSC system's components using computer simulation in this study. The impact of antimony, chlorine, nitrogen, and indium elements on the supercell structure of SnO_2 was examined using Density Functional Theory. The SnO_2 structure was doped with one or two elements using the substitution method, and then the structural, electrical, and optical properties were computed.

First-principle DFT calculations were performed using the CASTEP code [46], which employs a Vanderbilt-type ultra-soft pseudopotential and a plane wave expansion of wave functions. We used the GGA with the Perdew-Burke form (PBE) to represent the exchange and correlation potential [45]. The electron configurations represented by the pseudopotentials for the Sn and O atoms are $5s^25p^2$ and $2s^22p^4$, respectively. The integration across the first Brillouin zone was conducted using the Monkhorst-Pack approach with k-point sampling [46]. The bulk structure was taken into consideration as the reference for examining the impact of doping SnO_2 with various components. At 650 eV, the energy cutoff for plane waves was established. For the 7x7x8 k-point integration, we chose a grid tolerance that was $5.0x10^{-7}$ eV/atom for the self-consistency field, $5.0x10^{6}$ eV/atom for the maximum force, $1.0x10^{-3}$ eV/atom for the maximum displacement, and 0.05 eV, respectively, for the maximum stress. The band structure, DOS and optical properties.

4 CHAPTER FOUR

In this chapter, we presented the results of our simulations of various attributes along with their analyses. The molecular structures of the undoped and doped SnO_2, geometric optimization, and electronic and optical properties were studied using DFT with GGA, resulting in a method with better performance for use in DSSC.

4.1 Structural properties of SnO_2 that is both pure and doped.

4.1.1 Pure bulk and supercell structure.

Rutile, a tetragonal system structure with symmetry of D_4hI_4, is present in SnO_2 crystals. SnO_2 crystals have the following lattice parameters: β=γ=α=90°, a=4.74 and c=3.19 Å for unit cells, and a=9.48 Å and c=6.37 Å for supercells. Two molecules with tin and oxygen atoms are present in both the atomic cell and the supercell. Figure 6(a) and (b) respectively depict a unit cell and a 2x2x2 supercell.

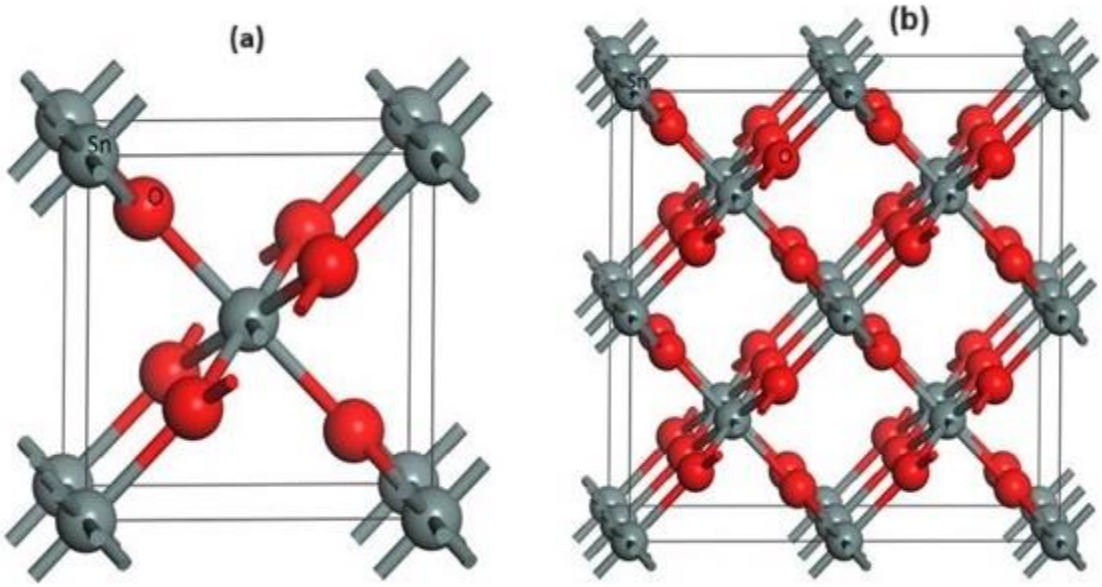

Figure 6: The tetragonal unit cell of SnO_2 (a) and 2x2x2 supercell (b).

Table 1 below shows contrast of the structure of SnO_2 supercells with bulk SnO_2. The outcomes support the approach taken in determining the structure's attributes. The calculated lattice parameters is in close agreement with the experimental findings of Batzil *et al* [48]. This demonstrates that the technique was sound.

Table 1:Lattice parameters for bulk and undoped supercell structure of SnO_2.

Lattice parameters		Literature[10-13]	Experimental [65]	This work	% Deviation
Bulk	a (Å)	4.74	4.74	4.68	1.20
	b (Å)	4.74	4.74	4.68	1.20
	c (Å)	3.19	3.19	3.19	0.30
Supercell	a (Å)	9.48	9.47	9.36	1.20
	b (Å)	9.48	9.47	9.36	1.20
	c (Å)	6.37	6.37	6.37	0.30

4.1.2 Doping mechanism.

The variation in the lattice can be ascribed to ionic radii of N, Cl, In and Sb. Where the ionic radii of N, Cl, In and Sb are 73 Å, 73 Å, 100 Å and 140 Å respectively. The atomic radius of oxygen is 73 Å and that of the Sn is 167 Å. When the substitutional doping was performed, the atomic radius was taken into consideration, O atom was substituted by N and/or Cl whereas Sn was substituted by In and/or Sb since they are radius related. This substitutional doping causes a little change in parameters b and c, and they maintain the morphology of the structure. Geometry optimizations were done for all scenarios, including both undoped and doped SnO_2, and the self-consistent courses ended when the force per atom was less than 0.03 eV/atom . Figures 8 and 9 below depict the doped SnO_2 structures. Table 2 lists the outcomes for undoped and doped structures.

4.1.3 Anionic doping of SnO2 with N and Cl and co-doping.

In case of N and Cl substituted into the SnO_2, they constitute to be the donor. Anionic doping was performed when oxygen was substituted with N and Cl. Non-metal doping affects the morphology of the structure by increasing or decreasing the lattice parameters. Figure 8(a), (b) and (c) show the substitutional doping of N, Cl and N-Cl into SnO_2 supercell. The lattice

parameters alter just a little of SnO_2. The lattice parameter contracts as a result of the large ionic radius of Cl, which is 100pm, and that of oxygen, which is 73pm. The results of lattice parameter are summarized in Table 2 below.

Table 2: Summarized results of undoped, doped, and co-doped SnO_2.

Lattice parameters	a (Å)	c Å)	The band gap (eV)	Electronegativity
N-SnO_2	9.08	6.07	3.22	
Cl-SnO_2	9.78	6.52	3.03	
N-Cl-SnO_2	9.27	6.02	1.93	
In-SnO_2	9.67	6.48	3.70	
Sb-SnO_2	9.33	6.08	3.18	
In-Sb-SnO_2	9.35	6.05	3.44	
			ionic radius(pm)	
O			73	3.50
N			73	3.00
Cl			100	3.00
Sn			140	1.80
Sb			140	1.90
In			167	1.70

Depending on the type of dopant, we can find the band variation. The band gap narrows when the anion is substituted inside the SnO_2. Similar to this, the band gap decreases when cationic

doping is applied. The co-doping method, whether cationic or ionic, produces the narrowest band gap except for In-SnO_2.

N and Cl ionic radii are summarized in Table 2 above. Substitutional doping affects the coulomb interaction between two ions since the force of attraction between molecules will either increase or decrease depending on the ionic radius. Large ionic radius results in an increase in the force of attraction or repulsion since they will be close to each other according to Coulomb's law, this result was evident by Colic *et al* [56].

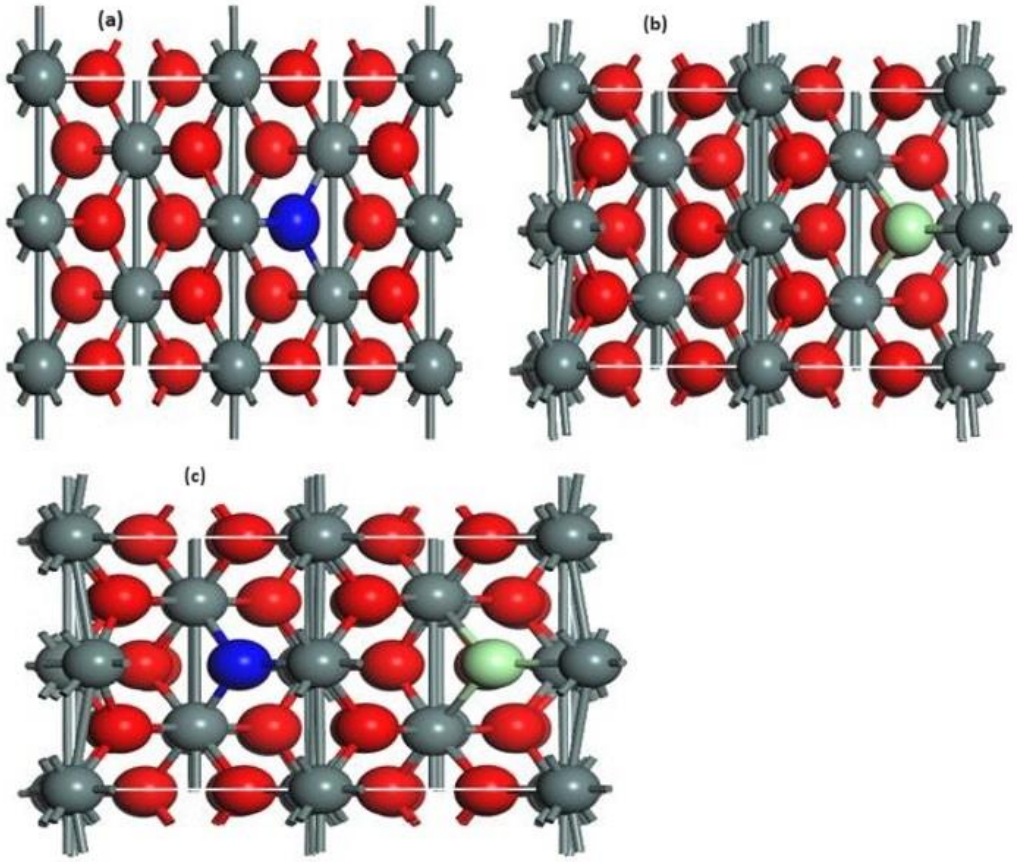

Figure 7: SnO_2 supercell doped and co-doped with (a) N, (b) Cl and (c) N-Cl.

4.1.4 Cationic doping of In and Sb and the co-doping.

The ions that make up metal doping are known as cationic doping. Figure 8 (a), (b), and (c) below shows the substitution of In and Sb, which replaced the Sn atom. The band gap is greatly influenced by cationic doping, which also has an impact on the CB of the structure. According to Li *et al*. the conduction band is altered by cationic dopants, which are typically

metal-type dopants. They further stated that because the dye molecules are bound to the cations, changing one cation with another often impacts the amount of dye that is anchored because the binding strengths of the dye molecules and the new cation elements are different [50]. There is a Coulomb attraction between Sn, In, and Sb when the Sn atom is replaced with either an In or Sb atom. The lattice parameter and volume are altered as a result. This is explained by a discrepancy in the polarity and ionic radius of the molecules [51].

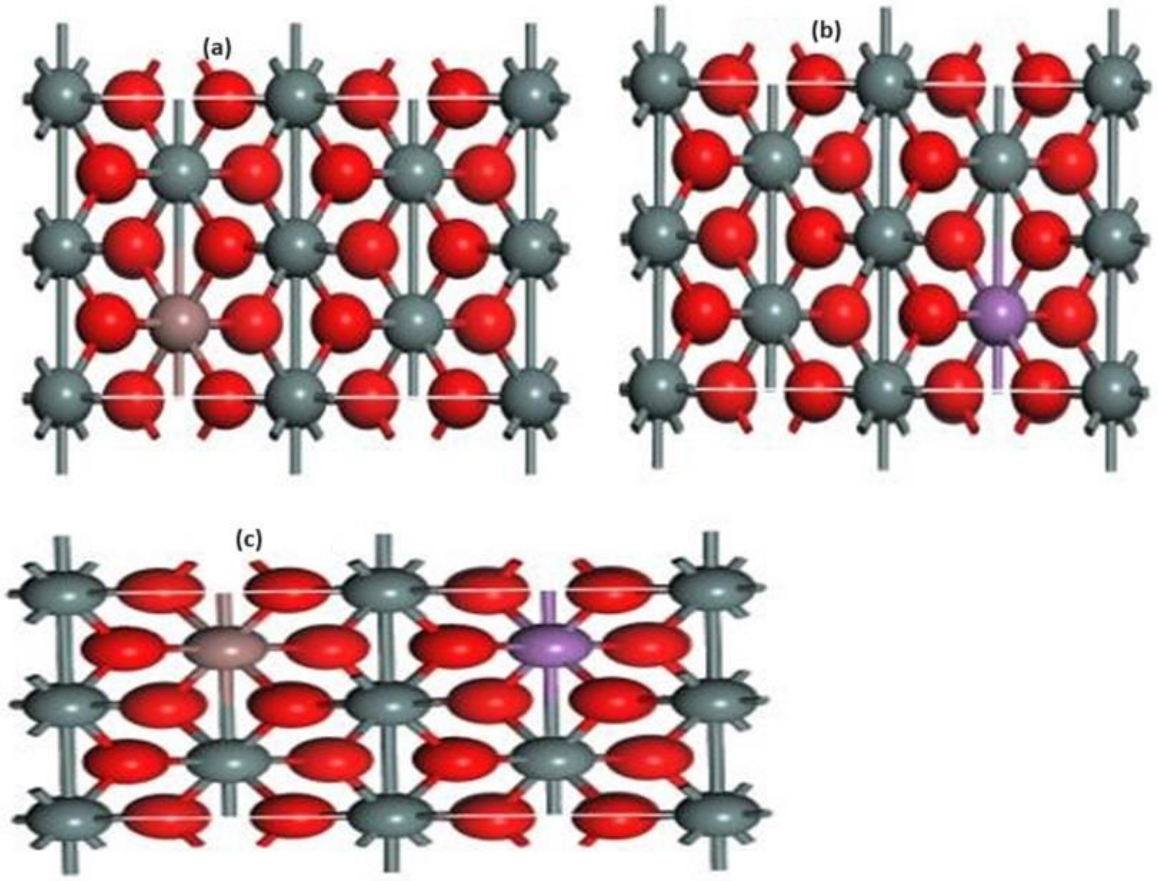

Figure 8: SnO_2 supercell doped and co-doped with (a) In, (b) Sb and (c) In-Sb.

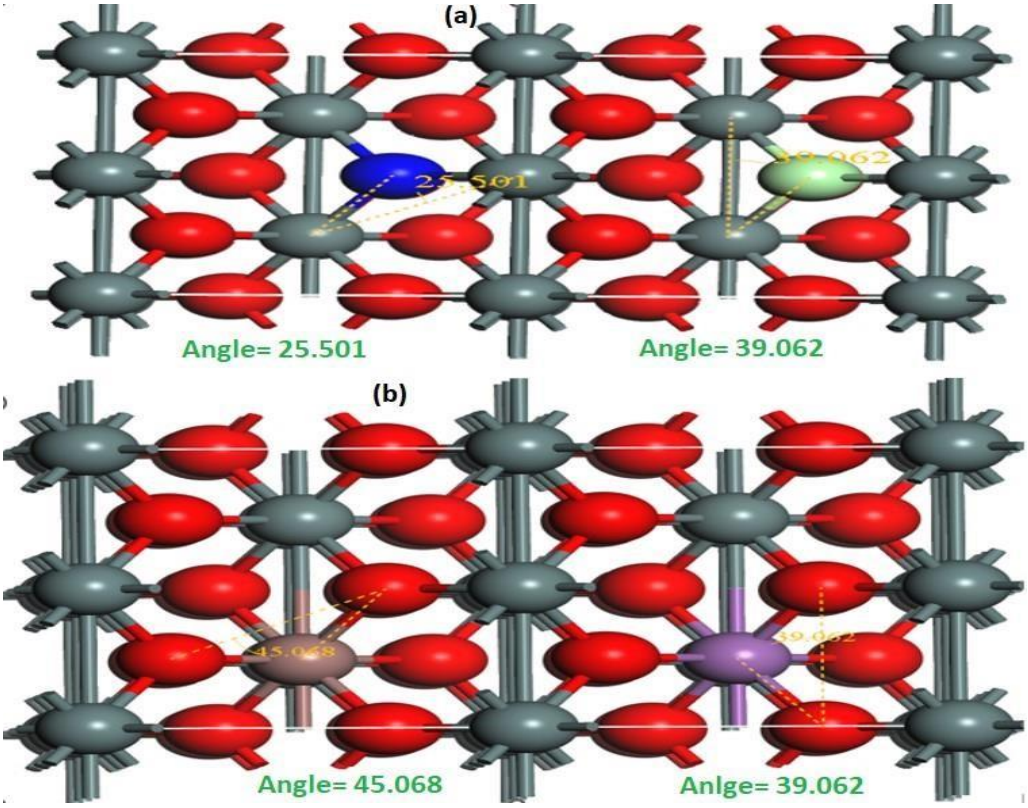

Figure 9: The angle between the (a) O-N, O-Cl and (b) O-In, O-Sb.

Figure 9 (a) and (b) above show the angle between O-N, O-Cl and (b) O-In, O-Sb when they are introduced to the SnO_2 structure. The bonding angles for N and Cl doping were discovered to be 25,501° and 39,062°, respectively. It is demonstrated that when In and Sb are used to replace Sn, the resulting angles are 45.068° and 39.062°, respectively. This is caused by the variation in ionic radius between our dopants.

4.2 Electronic properties of SnO_2 that is both pure and doped.

4.2.1 Pure unit cell and supercell of SnO_2.

Both the band structure and partial density of state were investigated and reported in

Figures 10(a) and (b), Figure 11 and Figure 12 below, respectively, to help in understanding of the electrical characteristics of the undoped SnO_2 bulk and SnO_2 supercell structures.

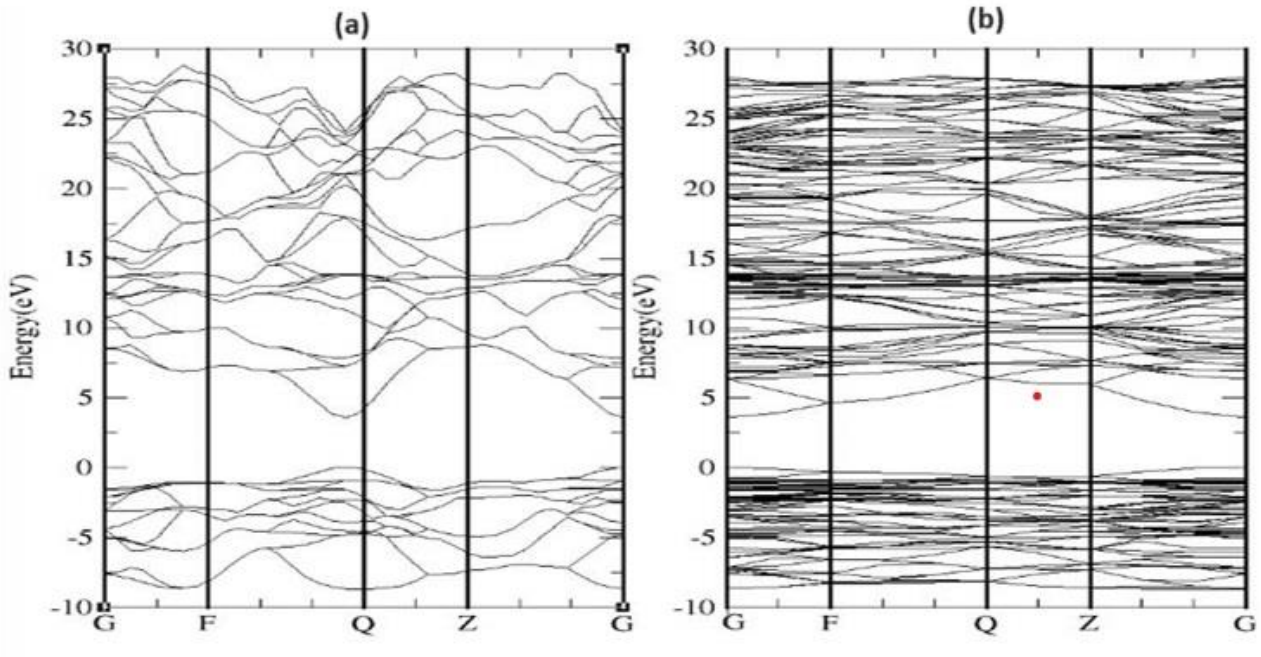

Figure 10: Band structure of SnO_2 unit (a) and (b) 2x2x2 supercell.

We looked at the estimated electronic properties of the undoped systems. The undoped structure was examined using the Perdew-Burke Ezrnzehof (PBE) technique, which allows the supercell parameters and atoms to relax until the forces on all atoms are covered. The band structures are defined along the high symmetry Brillouin zone path G-F-Q-Z, with the Fermi level set at 0 eV.

In the unit cell and 2x2x2 supercell, the VB and CB are both discernible, demonstrating that the devices are direct band gap semiconductors. The expected energy band gap discovered to be 3.6 eV and 3.57 eV, respectively, for the unit cell and supercell architectures. The calculated band gap coincides with the experimental band gap reported by Scheife *et al*. [52]. The states that are around the Fermi level were considered for computing the partial density

of state (PDOS). The CB is formed by the hybridization of O 2p and Sn 5s, which make up the majority of the valence band.

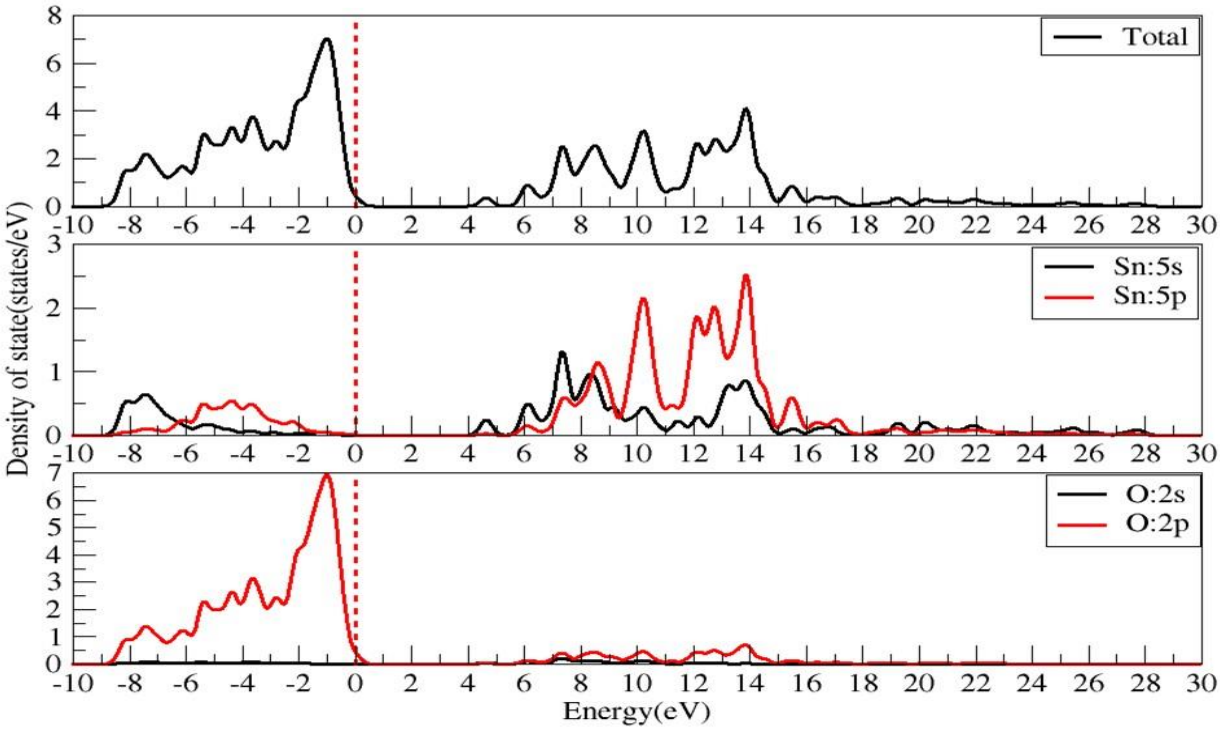

Figure 11: Partial Density of state of SnO_2 unit cell.

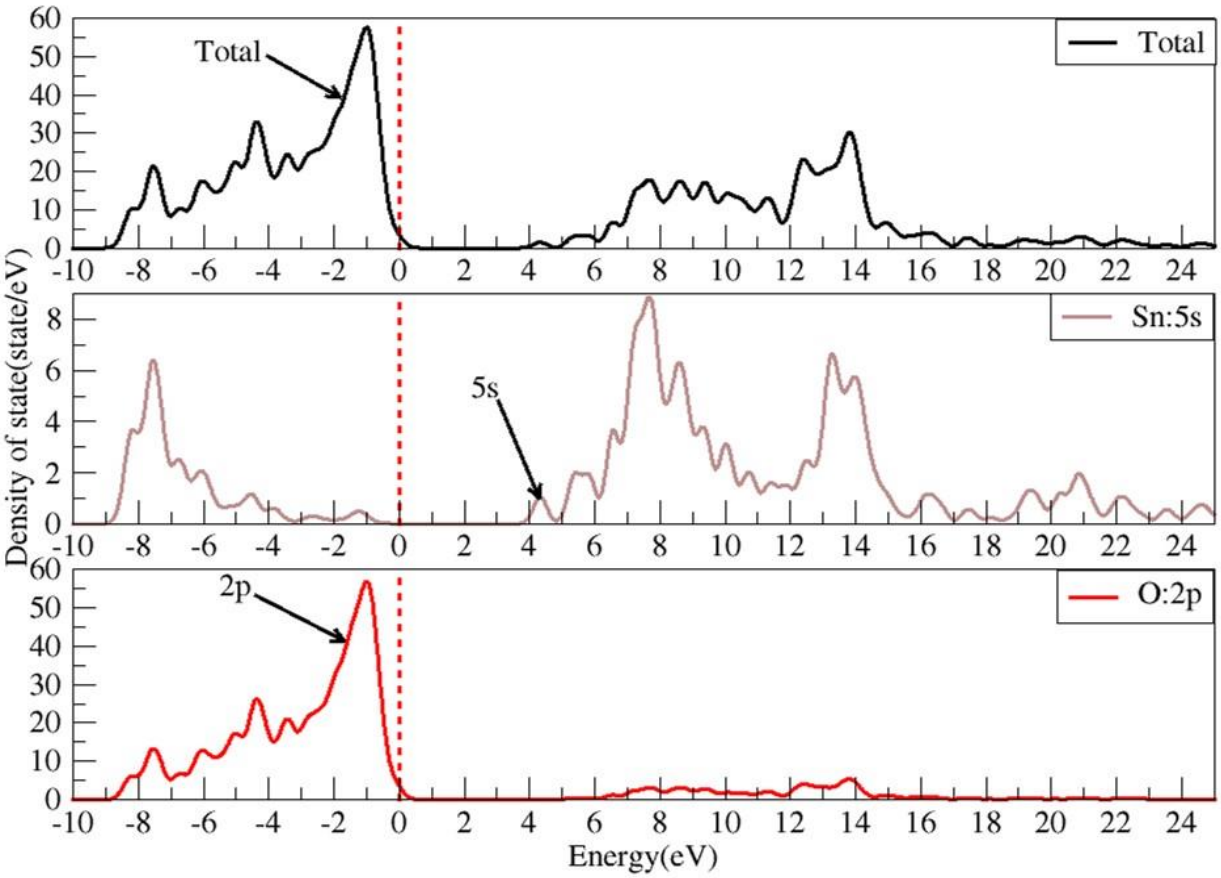

Figure 12: Partial density of state of SnO_2 supercell.

4.2.2 Calculated electronic properties of anionic doping of SnO_2 with N and Cl and the co-doping.

4.2.2.1 Mono-doping of N-SnO2.

A band gap reduction of up to 0.4 (3.6–3.22 eV) is depicted in Figure 13 below. The estimated band gap energy is 3.22 eV. Since both the CB and VB are located near the G point, it is obvious that N doped SnO_2 is a direct band gap semiconductor. Valence band is considerably altered by the addition of an anion to the structure. The conduction and valence bands' downward movement are what causes the n-type semiconductor [53].

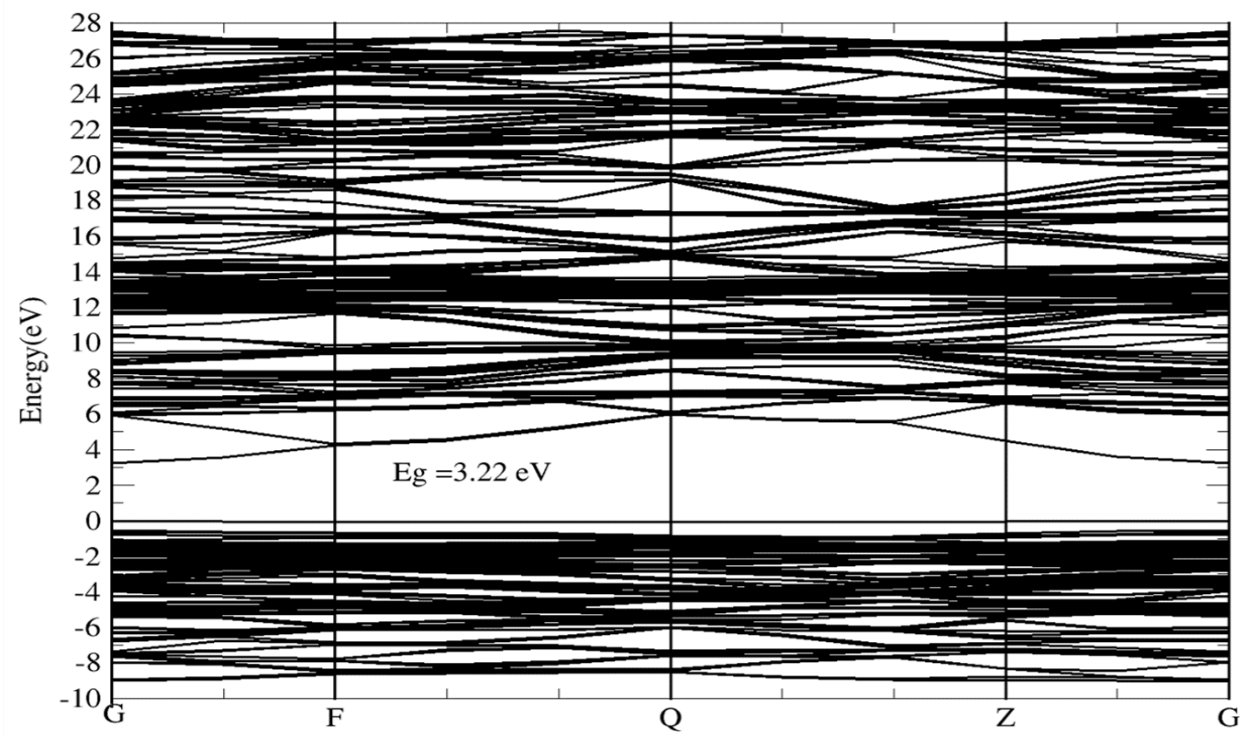

Figure 13: Band structure of N doped SnO_2.

The estimated partial density of states in Figure 14 below shows that the VB consists mostly of O 2p, Sn 5s, and N 2p orbitals, whereas the CB consists of orbitals with mixed Sn 5s and N 2p. The contribution of N 2p is represented by the peak at the Fermi level. It was also discovered by Luo *et al*. that gap state formation at the Fermi level may contribute to the electrical and optical properties of SnO_2, making it appropriate for PV and photocatalytic devices[53].

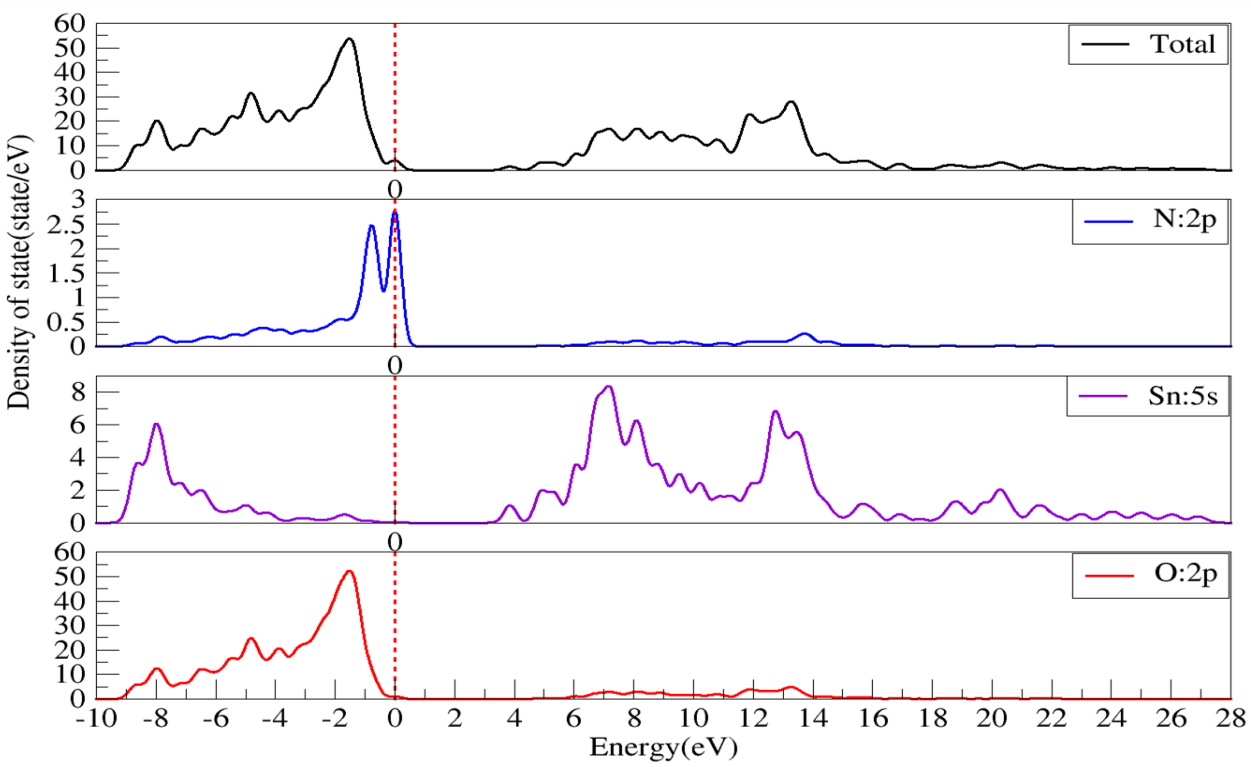

Figure 14: Partial density of state of N-SnO_2.

4.2.2.2 Mono-doping of Cl-SnO_2.

Figure 15 below shows the calculated band gap for Cl-SnO_2.The results show that the calculated band gap was 3.03 eV. The VBM and CBM are situated at G point. This also shows that straight band gap semiconductors are produced by SnO_2 doped with Cl. Strong interactions between Cl, Sn, and O can be attributed to shallow impurities within the band gap.

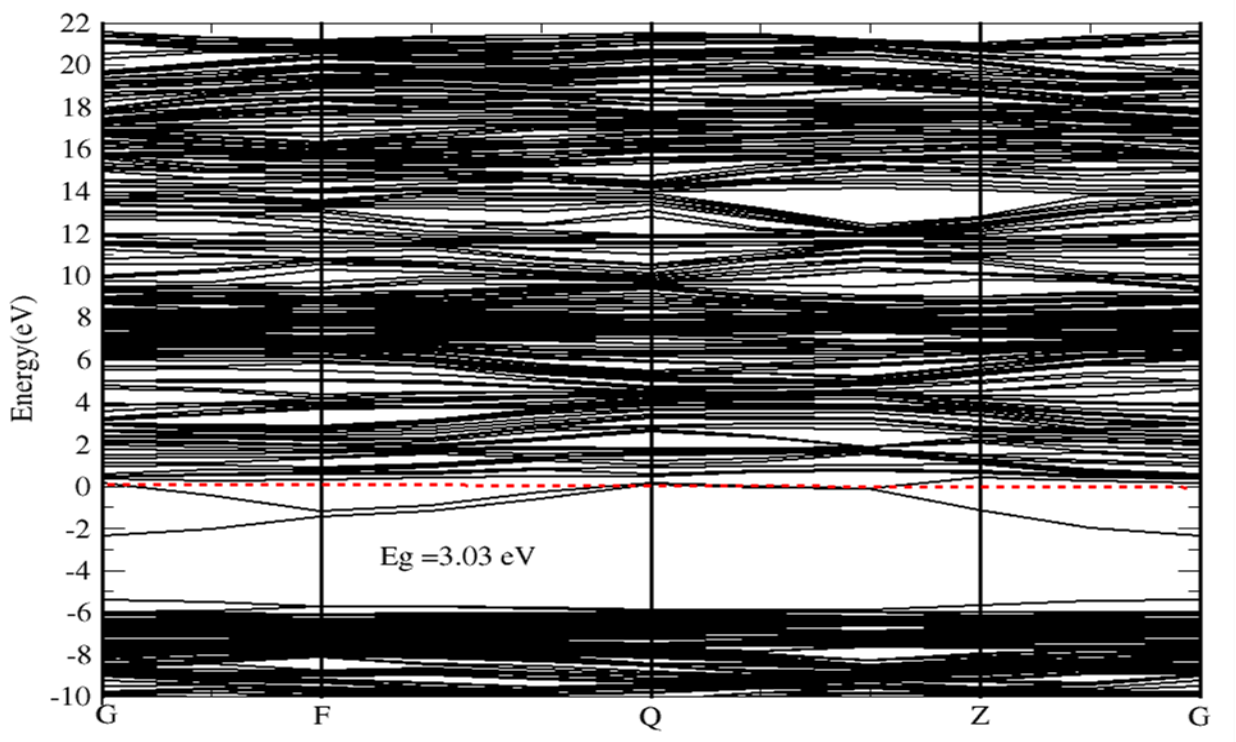

Figure 15: Band structure of Cl doped SnO_2.

According to Figure 16 below computed partial density of state, the VB is primarily made up of O 2p, Cl 3p, and Sn 5s, while the CB is a hybrid of the s and p states of O, Cl, and Sn. Cl 3p and O 2p interact with one another on the p-p level.

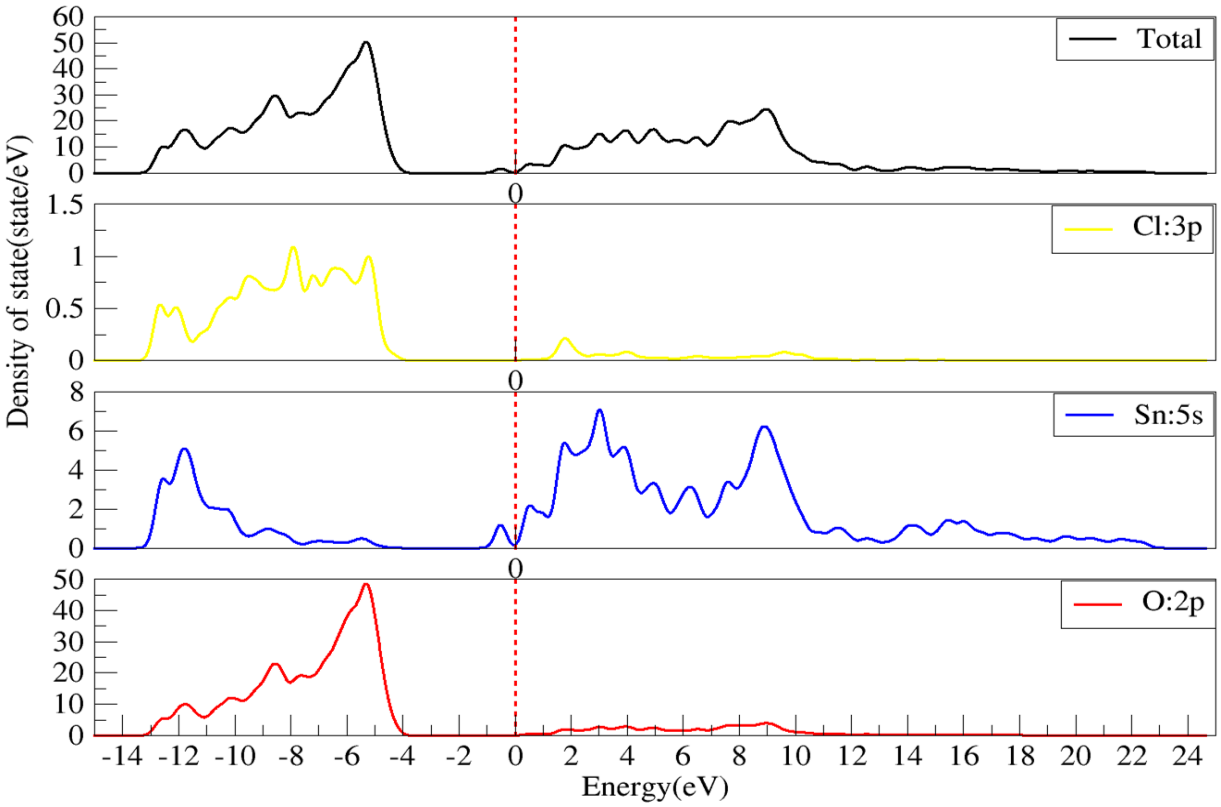

Figure 16: Partial density of state of Cl-SnO_2.

4.2.2.3 Co-doping of N and Cl SnO_2.

Figure 17 below illustrates the band gap for the N-Cl SnO_2 co-doping, which was determined to be 1.93 eV. According to a reduced band gap value of the doped systems compared to mono and undoped SnO_2, the band narrows as the ion concentration increases. When N and Cl were co-doped, the band gap was determined to be the smallest. The impurity energy levels (IELs), which are produced by hybridizing with O 2p states, Cl 3s and Sn 5s states, cause the co-doped SnO_2 to narrow its band gap. The IELs assist in the migration of photoexcited carriers and the photocatalytic process by aiding in the separation of photogenerated electron-hole pairs. Underneath the CB and overlapping with the VB are the impurity energy levels. These IELs may operate as photoexcited hole trap centres, slowing the rate of recombination. According to Dima *et al*. [54], co-doping and N-doping had the same outcomes.

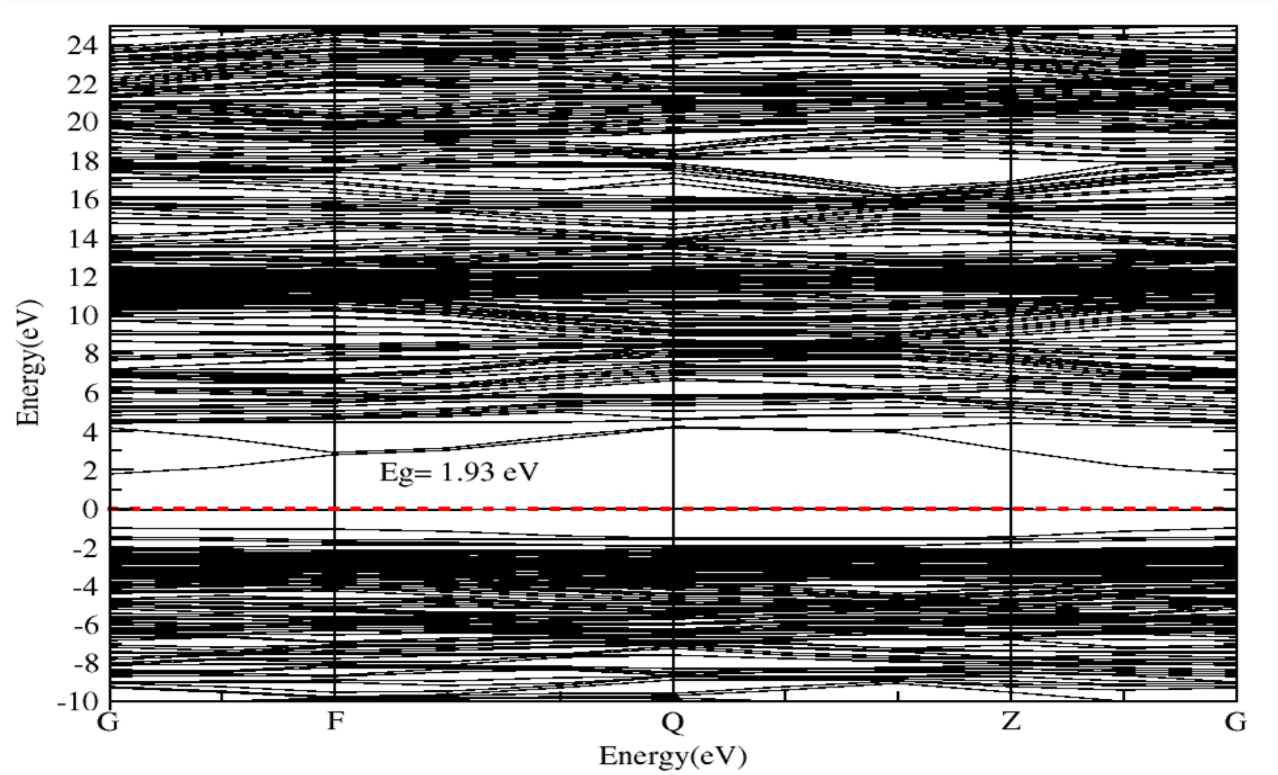

Figure 17: Band structure of N and Cl co-doped SnO_2.

Figures 18 below depicts the co-doped N and Cl SnO_2 system's anticipated density of state (PDOS). The partial density of states (PDOS) demonstrated that co-doping has little effect on the band gap of SnO_2 and that N and Cl cause impurities to exist within it. Figure 17 demonstrates that the band gap is 1.67 eV smaller than it was for SnO_2 that is not doped. These findings provide a justification for the experimental phenomenon that Yang *et al* [55], covered in their research. The band gap narrows when SnO_2 is doped, improving the material's photocatalytic properties.

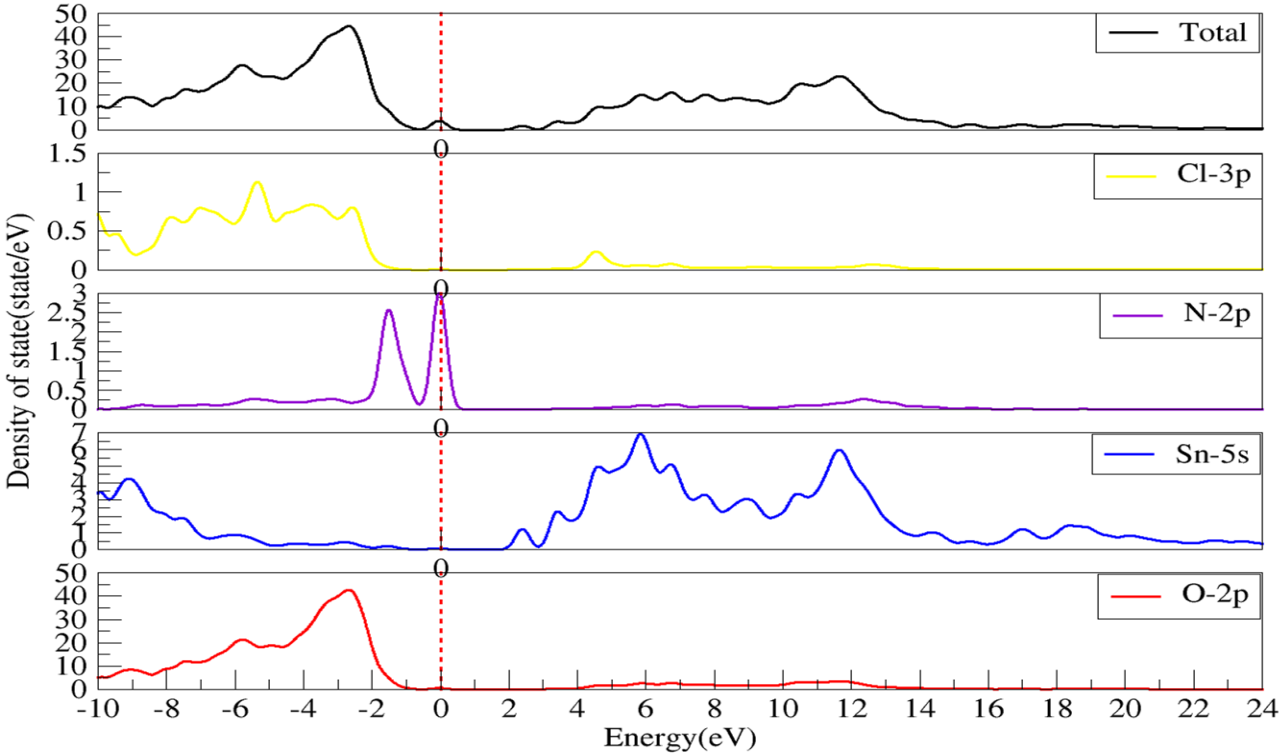

Figure 18: Partial density of state of N and Cl co-doped SnO_2.

Due to anionic doping, the N 2p and Cl 3s orbitals enhance the hybridization with the O

2s and Sn 5s states, however, to a considerably lesser extent than the O 2p state. At the G point, the VBM completely matches up with the conduction band minimum despite being slightly pushed downward at the same time. These results show that the gap state, which is at or in the Fermi level, introduced by doping SnO_2 with nonmetal, significantly affects the band gap there.

4.2.2.4 Cationic doping of In, Sb and the co-doping.

The substitution of metal ions in the structure is known as cationic doping. Metal doping is said to have a significant impact on the valence band. To alter the optical and photoelectrochemical characteristics of metal oxide semiconductors, several metal dopants have been added. According to S. Chayoukhi *et al*. doping SnO_2 with Co results in a minor change in the radius of Sn, which causes the lattice cell to contract and/or reduce the band gap [26]. Another study revealed that the band gap is reduced when an In atom replaces a Zr atom [27]. The findings of this study demonstrated that maintaining the valence maximum

potential while altering the band gap is primarily due to a conduction band minimum shift, which may be accomplished by doping In and Sb as cationic doping substitution.

4.2.2.5 Mono-doping of In-SnO_2.

Figure 19 below illustrates the calculated band gap value of indium doped SnO_2 as 3.70 eV. The conduction band decreased as it approached the Fermi level. This could result from in impurities forming a brand-new state in the band gap.

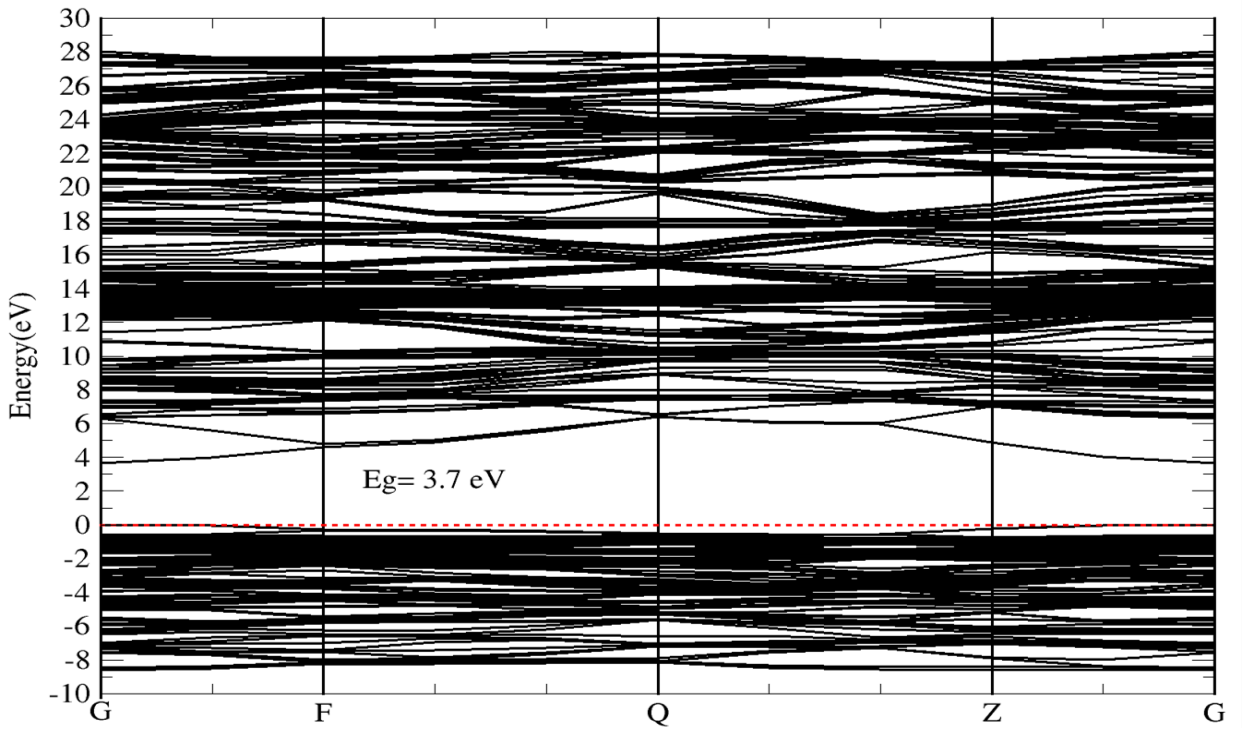

Figure 19: Band structure of In doped SnO_2.

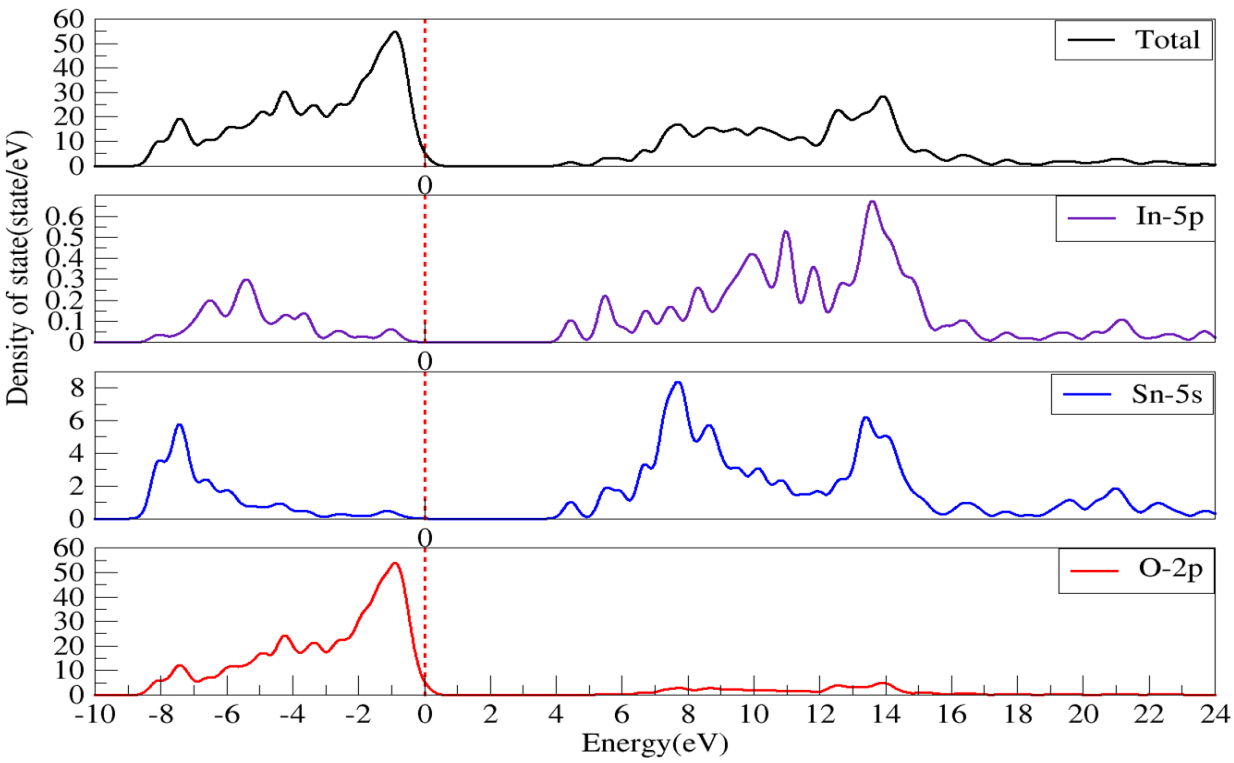

Figure 20: Partial density of state of In-SnO_2.

According to the computed partial density of state shown in Figure 20 above, In 5p makes a small but significant contribution to the conduction band. Since the treatment of In 4d electrons causes the hyper-deep band to lie very distant from the Fermi level, it was not considered. The peak that results from the hybridization of the states of In, Sn, and O is created from the overall density of states. Most of the In 5p states are located in the conduction band, with a little amount fading into the valance band. Thus, the conduction band contains only In-5p states. The outcomes showed that adding In considerably changed the electrical characteristics of SnO_2. By doping Sn with substituted elements, a novel state close to the Fermi level has been discovered.

4.2.2.6 Mono-doping of Sb-SnO_2.

The estimated band gap was discovered to be 3.18 eV, as shown in Figure 22. The n-type semiconductor is now visible thanks to a downward shift in the CB. The band gap is narrowing, which is favourable for electron mobility. The photoanode will accelerate more ejected electrons, which will slow down the rate at which electrons from CB and VB

recombine. Reduced band gap is beneficial for use in DSSC, this was determined by comparing the findings to those of Ma *et al* [56] .

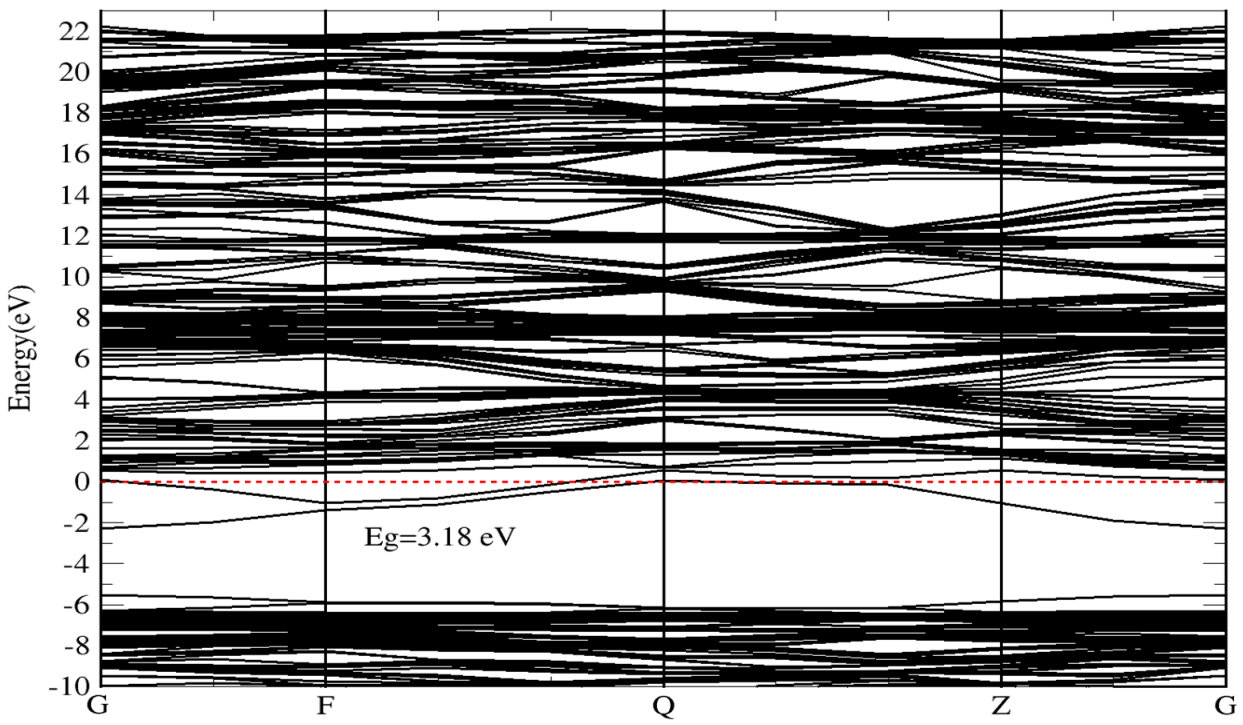

Figure 21: Band structure of Sb doped SnO_2.

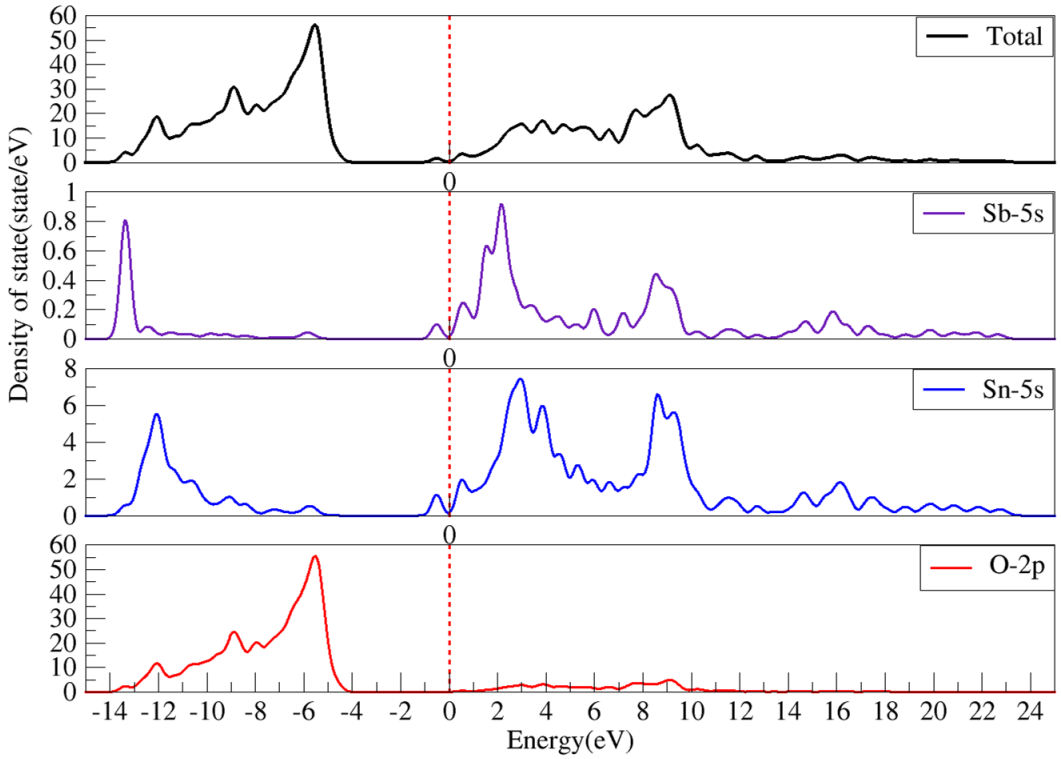

Figure 22: Partial density of state of Sb-SnO_2.

The predicted band structure and PDOS of Sb-doped SnO_2 are displayed in Figures 21 and 22. Tran *et al*. suggested that doped SnO_2 represents direct band gap [16], and the computed findings demonstrate a gap of 3.18 eV. Sb 5s are responsible for the states that are introduced within the band gap; by looking at the total density of states, we can easily understand how each of these states contributes. The hybridization of Sb 5s and Sn 5s states with a little amount of O 2p states results in peaks that are close to the Fermi level. The band gap was reduced as a result of the strong Coulomb force produced by the interaction between Sn 5s and Sb 5s, which caused the state of Sn to migrate down to the Fermi level. The Sb impurity-introduced carrier has a significant localization feature and is stuck in the acceptor level towards the top of the VB. Furthermore, around the Fermi level, the Sb states contribute more.

4.2.2.7 Co-doping of In-Sb-SnO_2.

Figure 23 below shows a gap of 3.44 eV for co-doping of In and Sb on SnO_2. According to Filippatos *et al.* [33], both the CBM and the VBM are found near the G point. With the exception of where the Fermi level is located, the total DOS of SnO_2 varies only slightly when Sn and In are substituted in the supercell. The effect of this extra electron, which also exposes

an n-type semiconductor, is confirmed by the fact that Fermi level is at the top of the valence band. The summits, though, melt together. The resulting VB-DOS is a little more complicated than a pure supercell in terms of its properties. Keep in mind that the uppermost valence band of the pure supercell has a relatively modest dispersion. The resulting effective band gap agrees well with the experimental findings that have been published. The outcomes presented by Ammari *et al.* [57] also support this.

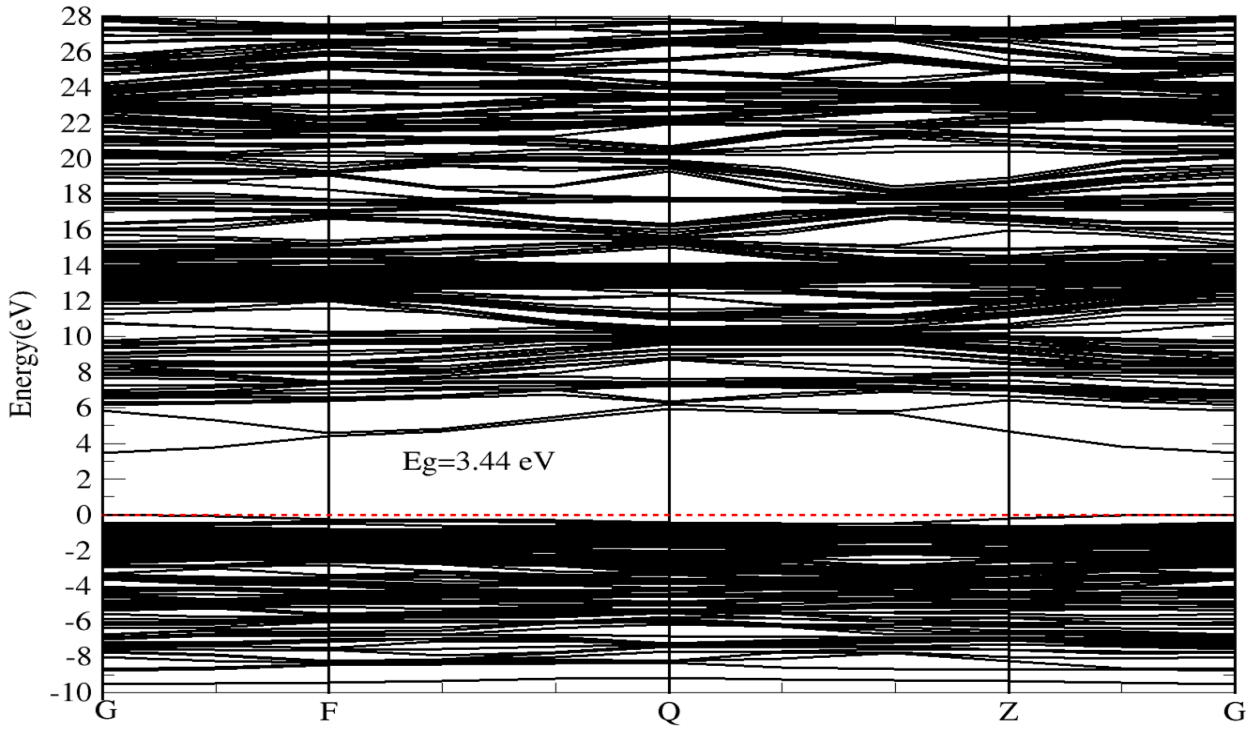

Figure 23: Band structure of In and Sb co-doped SnO_2.

When Sn is replaced by In and Sb, the concentration of the Sn cation is lowered, as seen below in Figure 24 below which consolidates the contribution of the In 5p and Sb 5s states. The novel state contributed by In 5p and Sb 5s is introduced when these two ions are co-doped, and this is consistent with other electrical features noted by Ammari *et al.* [57].

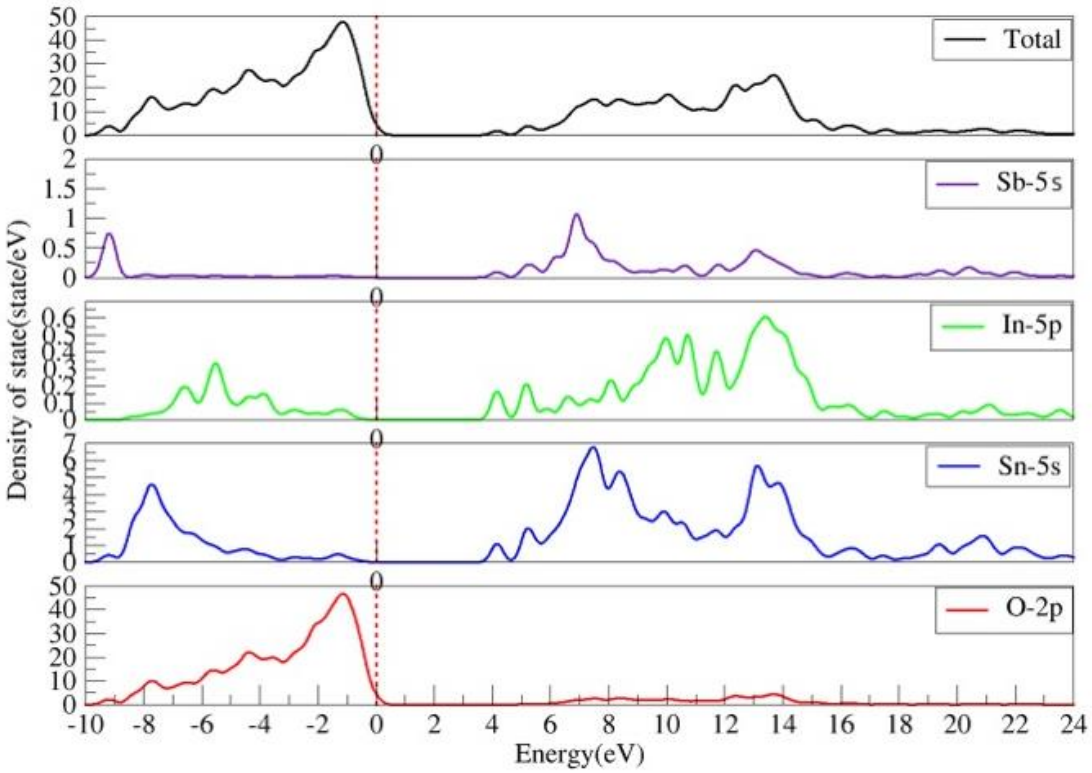

Figure 24: Partial density of state of In and Sb co-doped SnO_2.

In summary, the electronic properties were calculated. Subsequently, it was found that anionic p and s states and cationic p and s states, generate VBM and CBM respectively .The d states in cationic doping were not considered because they are deep or very far from the Fermi level. The p states naturally have a smaller slope than the d states close to the extrema as well. Surface-reaching electrons are more likely to arise under light irradiation than surface-reaching holes because of the significantly larger mobility of electrons in the VB compared to holes in the CB . Our results show that increased activity is governed by electrons, which will improve the performance of the devices because the majority of photocatalytic activities are controlled by holes involved in oxidizing half processes . Additionally, Yang *et al* [55] showed that the band gap width and electron mobility are fundamentally associated, the higher the mobility of electrons, the smaller the band gap. The effective hole transmission and charge separation that are promoted by expanding the VB width have a direct impact on the unbalanced mobility of holes and electrons.

4.3 Calculated optical properties of SnO_2 that is both pure and doped.

4.3.1 Mono doping and co-doping N, Cl, In, and Sb.

4.3.1.1 Absorption.

The absorption coefficient reveals the material's capacity to transform solar energy, as well as the depth to which light of a particular frequency may travel before it is absorbed. The disparity between the energy levels of an electronic transition can be used to describe the energy and wavelength of absorption. The absorption coefficient A is related to the extinction coefficient k, by the formular:

$$\alpha = \frac{4\pi k}{\lambda} \quad \text{.....(24)}$$

Where λ is the wavelength, if is nm, multiply by 10^7 to get the absorption coefficient in the unit of cm^{-1}.The optical absorption spectra of doped and undoped materials were computed to examine the absorption properties, and the results are displayed below in Figure 25 below. Knowing that the band orientation of SnO_2 is affected by the presence of N, Cl, In, Sb, and N-Cl impurities. Analysing how dopant's impurities impact optical characteristics is important.

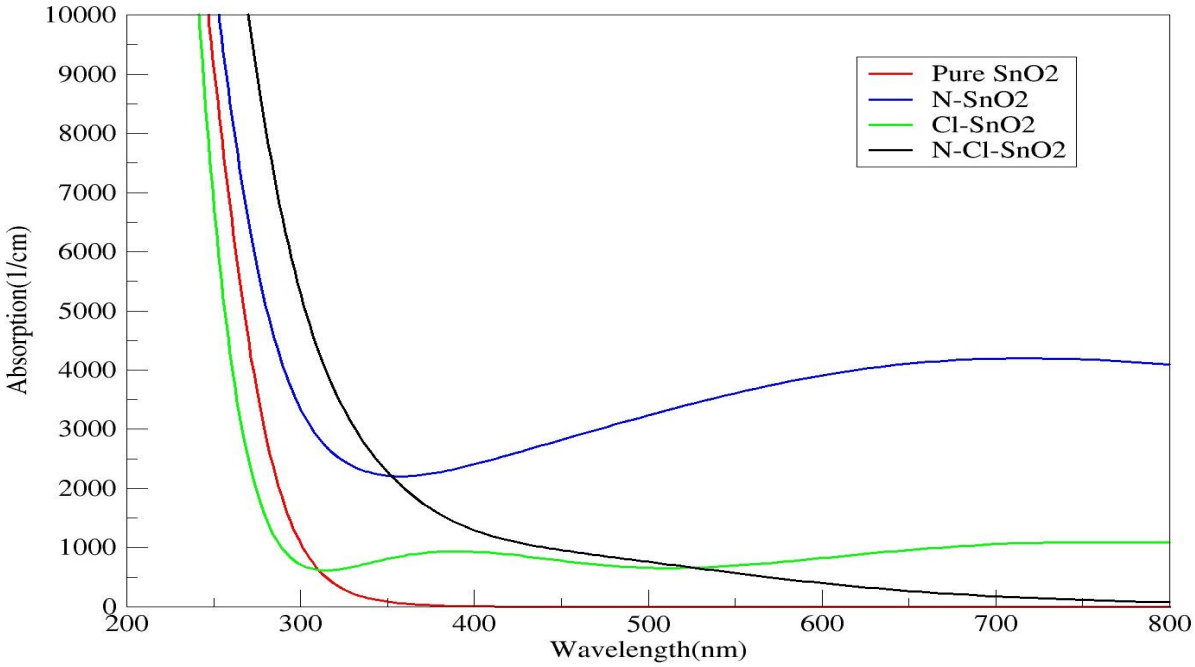

Figure 25: Calculated optical absorption for doped and undoped SnO_2.

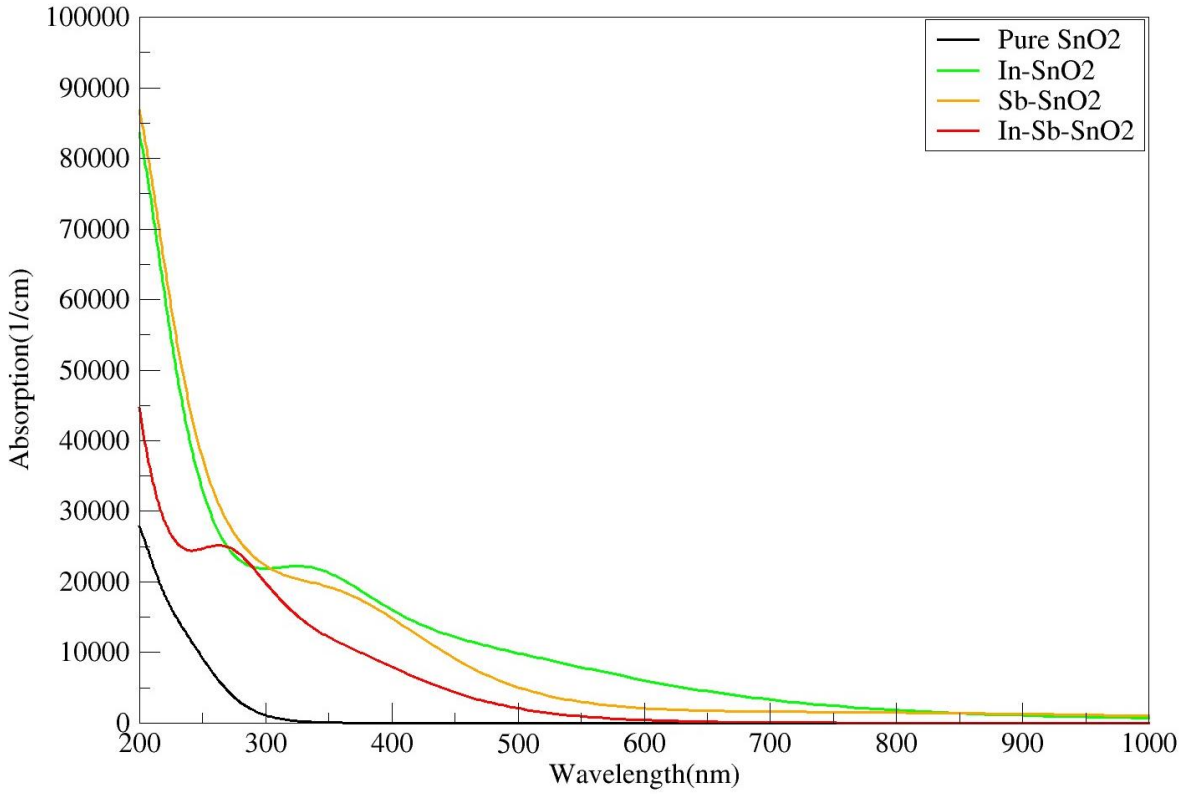

Figure 26: Calculated optical absorption for doped and undoped SnO_2.

There is a noticeable migration from the lowest frequency to the highest frequency on the optical absorption side. According to this, the optical band gap of doped SnO_2 altered somewhat in contrast to an undoped SnO_2 system, even though the band gap of SnO_2 shrank after doping.

The data presented above in Figure 26 and 27 showed that the maximum values of the absorption coefficient increase in the mono-doped of N compared to Cl, and in the mono-doping of In compared to Sb structures within the range of 400 nm to 800 nm. The absorption peaks shift to higher energy and show a slight red shift as shown in Figure 26 and 27. Similar results were previously presented by Luo *et al.* [53]. This phenomenon means that the doped SnO_2 absorption increases when mono-doping was employed as there is a slight increase in the absorption coefficient and during co-doping the absorption activities are higher than the undoped SnO_2. While the co-doping of In and Sb shows only a very rise to higher than N and

Cl doping wavelengths, the mono-doping and co-doping of N and Cl has boosted the absorption to a higher wavelength but with the smallest absorption coefficient. Therefore, the absorption increases when mono-doping is employed better relative to co-doping in the case of cationic doping. The calculation of the optical absorption revealed that these doped SnO_2 have shifted the absorption coefficient to higher energy range . In conclusion, the small band gap's strong light absorption and the multiple scattering effect help to increase the production of photogenerated electrons and holes. The photocatalytic reaction can involve more holes and electrons, improving photocatalytic activity because SnO_2, a doped direct semiconductor, has a lower recombination rate for photogenerated electrons and holes than an undoped direct semiconductor.

4.3.1.2 Energy loss function.

Peaks in the electron energy loss function, are a key optical parameter that indicates how much energy fast electrons lose when traveling through a material, are related to plasma resonance characteristics. Peaks in loss function spectra's positions, which coincide with the so-called plasma frequency, also draw attention to how all materials' attributes transition from metallic to dielectric. The energy loss function of energy (w) and momentum transfer (q) is given by the imaginary part of the reciprocal of the complex dielectric function $\varepsilon(\omega, q)$. Using the energy loss function (ELF) and Born approximation , the differential inelastic scattering cross section ,per atom or molecule ,for energy loss ω and momentum transfer q in an infinite medium is given by:

$$\frac{d^2\sigma}{d\omega dq} = \frac{1}{\pi NE} Im\left[-\frac{1}{\varepsilon(\omega,q)}\right]\frac{1}{q} \quad \text{.....(25)}$$

where E is the electron energy and $Im\left[-\frac{1}{\varepsilon(\omega,q)}\right]$ is the ELF ,which is now defined by the complex dielectric function [54].

Figure 27 below, the loss function of undoped and doped SnO_2 structure exhibits peaks at 0-3 eV and undoped SnO_2 does not have any activity within that range, which correspond to the abrupt drop and constant value of reflectivity, respectively. For doped SnO_2, there are three large peaks at 30 eV of which this correspond to higher wavelength, and it will results in the lowest frequency, this is show the decline in reflectance from the beginning to the end.

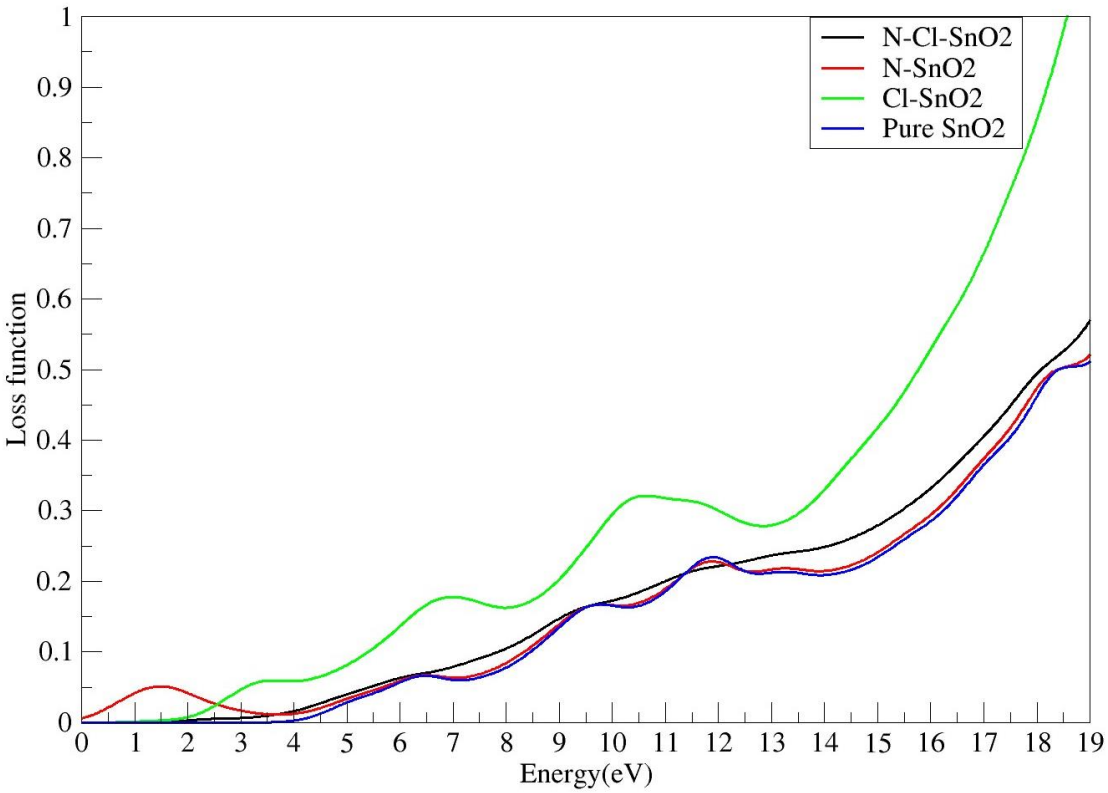

Figure 27: Calculated loss function of N, Cl and co-doped SnO_2.

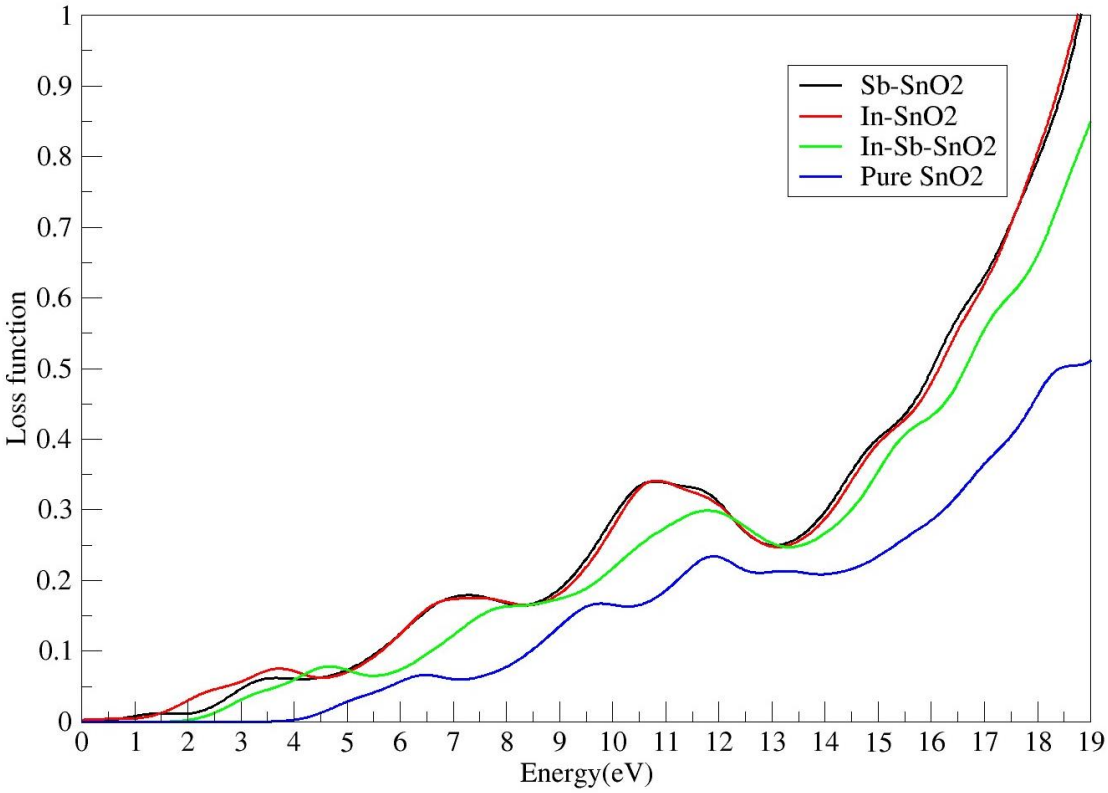

Figure 28: Calculated loss function of In, Sb and co-doped SnO_2.

Figures 27 and 28 above show the calculated loss of function of both anionic and cationic doping. Mono doping of N, Cl, In and Sb showed high energy loss of In compared with the co-doped and undoped systems. Between 0-3.6 eV, there is a very high energy loss depicted by both co-doped and undoped structures, this was also reported by Luo *et al.* [53]. The undoped structure does not show any activities under visible light. These results show that a large amount of energy will be reflected in the UV region than in Vis region since in the Vis region there are little activity of loss function, and this can measure the propagation loss of energy inside the medium or the material. For both doped and undoped SnO_2, the greatest peaks span from 4 eV to 38 eV. Both undoped and co-doped devices experience energy loss when the absorbed photons have higher energy than the threshold frequency. The energy loss values of undoped and co-doped materials mainly occur in the UV range because SnO_2's high band gap restricts its absorption to that area more.

4.3.1.3 Reflectivity.

Reflectivity is the percentage of incident electromagnetic power that is reflected at a contact, as opposed to reflection coefficient, which is the ratio of the reflected incident electric field. The refractive index is given by:

$$n = \left[N + (N^2 - n_0^2 n_1^2)^{\frac{1}{2}}\right]^{\frac{1}{2}} \text{ with } N = \frac{n_0^2+n_1^2}{2} + 2n_0 n_1 \frac{T_{max}-T_{min}}{T_{max}T_{min}} \quad \text{.....(26)}$$

where n_0 is the refractive index of air and n_1 is the refractive index of the substrate.

The internal reflection effect can make the reflectance change with surface thickness when reflection occurs from thin layers of material. Since reflectivity is the intrinsic reflectance of the surface and the limit value of reflectance as the sample gets thicker, it is unaffected by other factors like the reflection of the back surface.

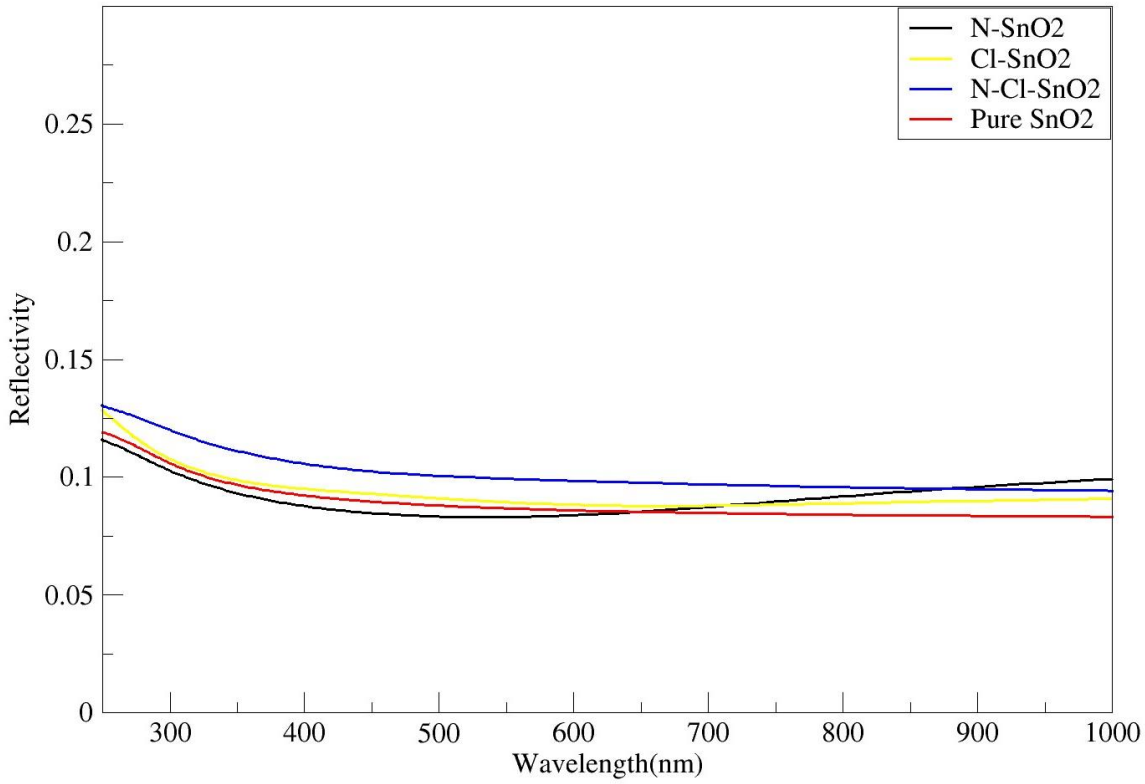

Figure 29: The reflectivity of doped and undoped SnO_2.

The optical reflectivity of undoped SnO_2 is low. In terms of co-doping, the optical reflectivity is higher than that of undoped SnO_2 in the visible spectrum but lower than that of mono-doping.

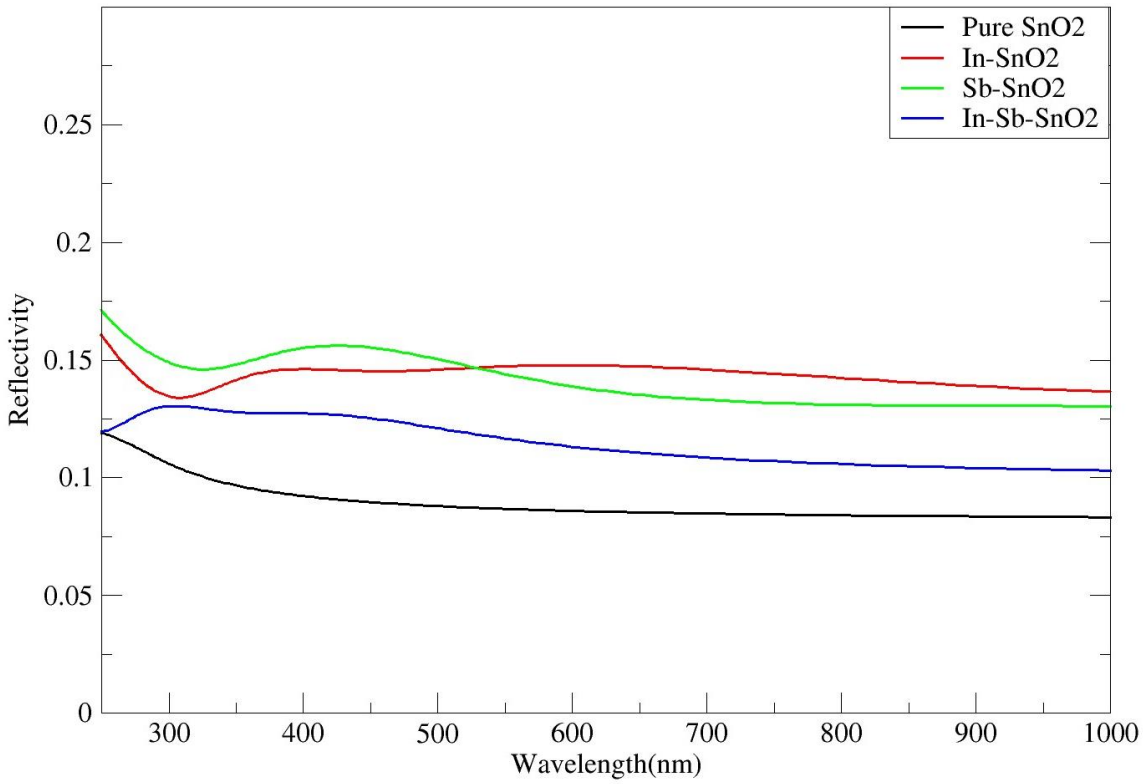

Figure 30: The spectra of SnO_2 with and without doping in terms of optical reflectivity.

The optical reflectivity spectra of doped and undoped SnO_2 are depicted in Figures 29 and 30. In the infrared, visible, and ultraviolet spectrum. The visible part of the spectrum has low reflection, which indicates good optical transparency. The structure which has high reflectance in the visible region is the In-SnO_2 this is due to its contribution to the PDOS of the structure, only few states of In where present. The undoped structure has higher band but its reflectivity is very low compared to the doped structure, This is to the mobility of the atom within the structure.

4.3.1.4 Dielectric function.

4.3.1.4.1 Real part of the dielectric function.

Figure 32 below depicts the doped and undoped structure's dielectric function. According to Anas *et al*. electron excitation and electron mobility are related to the peak of the real section of the dielectric function [27]. Analytical expression of the dielectric function is as follows:

$$\varepsilon(\omega) = \varepsilon_1(\omega) + i\varepsilon_2(\omega) \text{ ….…………………(27)}$$

The dielectric function is closely related to the electronic band structure. It fully describes the optical properties of any homogeneous medium at all photon energies. The imaginary part $\varepsilon_2(\omega)$ of the complex dielectric function is obtained from the momentum matrix elements between the occupied and unoccupied electronic states. It is calculated using the analytical expression in Equation (28):

$$\varepsilon_2(\omega) = \frac{2e^2\pi}{\Omega_{\varepsilon_0}} \sum\nolimits_{k,v,c} |\langle\psi_k^c|\hat{u} * \vec{r}|\psi_k^v\rangle||^2 \delta(E_k^c - E_k^v - E) \text{……………………………..(28)}$$

where ω is the frequency of light, e is the electronic charge, $\hat{u}$ is the vector defining the polarization of the incident electric field, ψ_k^c and ψ_k^v are the conduction and valence band wave functions at *k* respectively.

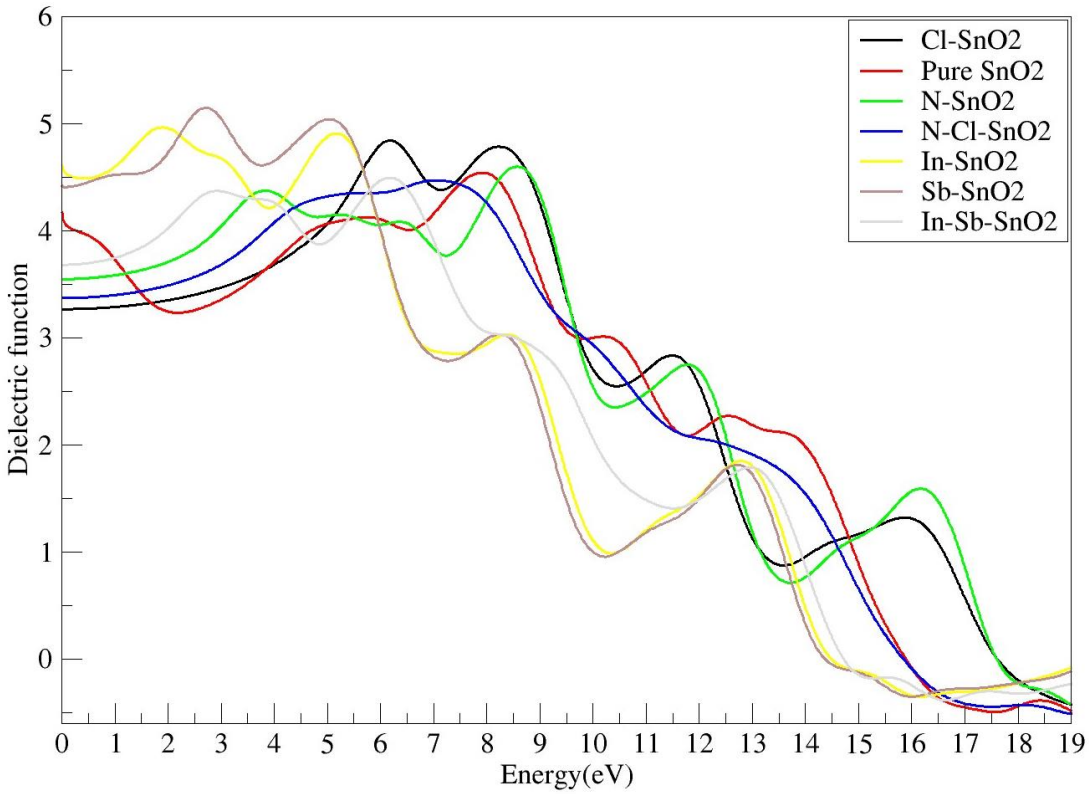

Figure 31: Real part of the dielectric function.

The greatest peaks for N, Cl, In Sb and N-Cl, In-Sb are displayed in the range of 0 eV to 10 eV for both undoped and doped SnO_2. All the systems were discovered to have maximal peaks in the UV region that start to decline at 19 eV. In contrast to co-doping and undoped SnO_2, mono-doping demonstrated an increase in the dielectric constant. The dielectric constant for N and Cl doping was calculated to be 3.26 and 3.51, respectively, whereas the values for co-doping and un-doping were 3.60 and 3.42, respectively.

In the case of In and Sb the dielectric constant was computed to be 5.1 and 4.49, for both for co-doped and undoped was calculated to be 4.2 and 3.6, respectively. Therefore, the dielectric constant of mono doping is higher than that of co-doped and undoped SnO_2.

4.3.1.4.2 Imaginary part of the dielectric function.

The features of absorption are closely related to the imaginary portion of the dielectric function.

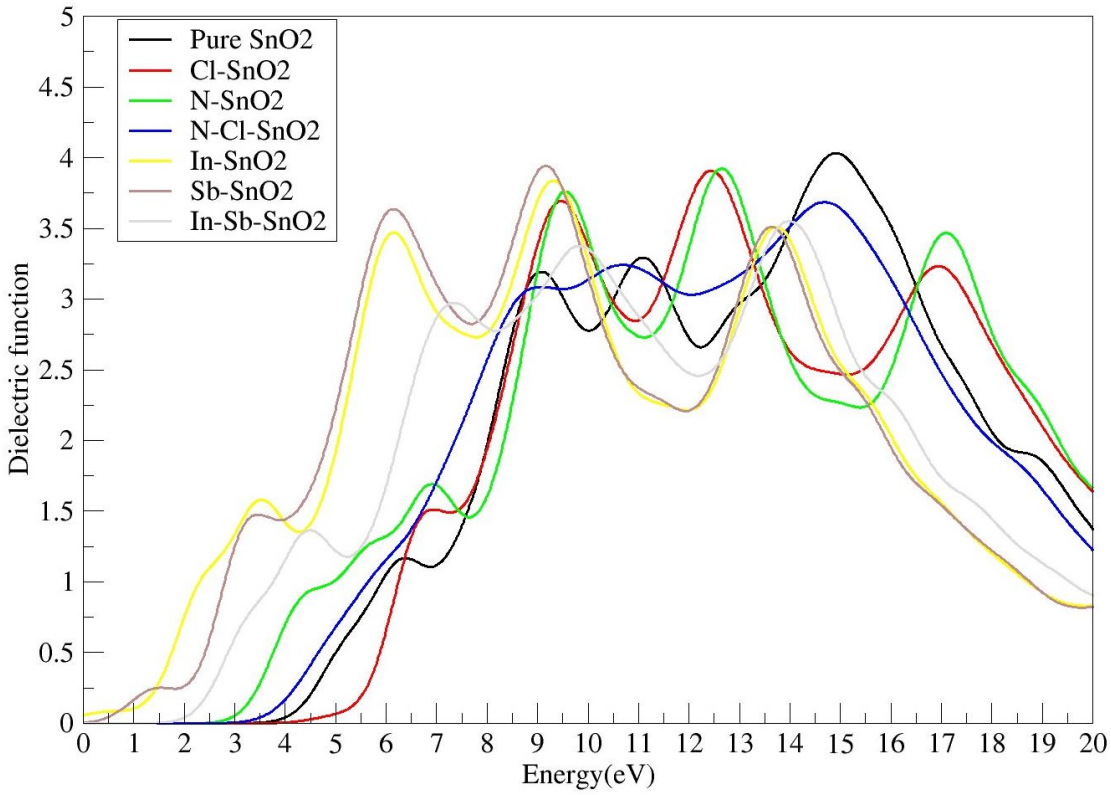

Figure 32: Imaginary part of the dielectric function.

It is found that the maximum value of dielectric increased in the doped structures as indicated in Figure 32 above. At the range 0-2 eV, In-SnO_2 has the highest peak, at Sb-SnO_2 at 1-2 eV. Cl, In, Sb showed the highest peaks while co-doping and pure show the low peaks. The peak for anionic doping and undoped SnO_2 increased in the range 15-18 eV as it is visible in Figure 32 above. At 32-45 eV In, Sb and Cl showed activities that are higher than those of undoped, In-Sb, N-Cl and N. These peaks are attributed to the transition between Sn-5s, the lowest conduction band, and O-2p, the highest valence band. The density of states can also be used to explain the various peaks. The transfer of the electron from the p state of the dopant states in VB to the p state in CB causes the peak to appear. According to Hossain *et al*. the dielectric function is a crucial indicator for determining the optical and electrical properties of materials [59]. The calculated dielectric function of a doped tin oxide confirms that there will be electron transition in the visible region (1.8 eV), this is reinforced by the small peaks in that region leading to the improvement of the photocatalytic activity of the material that is also suitable for application in DSSC cells.

5 CHAPTER FIVE

5.1 Conclusion.

Density Functional Theory and generalized gradient approximation with Perdew Burke Ezernzehof functional were used to analyse the structural and electrical properties of anionic (N and Cl) and cationic (In and Sb) doping of SnO_2 supercell. The results from theory and experiment were in good agreement with the calculated structural and electrical properties of SnO_2. The results showed that the lattice expands when Sn and O are replaced by In, Sb, and N, Cl, respectively. This structural distortion of SnO_2 is caused by the greater ionic radii of our dopants. It was discovered that when the number of dopants increased, the estimated band gap shrank. Furthermore, it was established that anionic doping is advantageous in lowering the band gap but poor in the absorptivity between cationic and anionic doping. These results are in accordance with Samanta *et al*. lead to reduced electron recombination and increased electron mobility [11]. The new states were created close to the Fermi level because of the various valence states of the dopant elements, which causes a narrowing of the energy band gap. According to the total density of the states, the Sn 5s and O 2p dominate the valence band, whilst the p and s states of the dopant dominate the conduction band. The slight alterations in the conduction band and band gap led to changes in the optical spectra of the doped SnO_2 structure in the visible region.

In this work it was demonstrated by the undoped system's larger energy loss function than the doped SnO_2 system. This is in line with optimal study that was reviewed which established that doped SnO_2 transmits light. Changes in the dielectric function, reflectivity, loss function, and absorption in the visible and end near-infrared are thought to be responsible for the transition from the occupied state to the empty band close to the Fermi level as well as the exciton effect. The optical characteristics of SnO_2 can be improved through doping.

The CB of SnO_2 is disrupted by nitrogen, a superior anionic dopant among non-metal ions, and electron recombination is hampered by nitrogen's high electronegativity. The influence of metal and non-metal doping, in particular, on electrical behaviour, drives us to design a semiconductor material with customizable electrical properties that may be applied in DSSC.

6 REFERENCES

1. S. Anandan, Y. Ikuma, K. Niwa. An Overview of Semi-Conductor Photocatalysis: Modification of TiO_2 Nanomaterials. Solid State Phenomena, vol. 162, pp. 239-260, 2010.
2. H. Joffe. Challenges for South Africa's Electricity Supply Industry. Helen Suzman Foundation Focus, vol. 64, pp. 32-37, 2012.
3. O. Mounkachi, E. Salmani, M. Likhal, H. Ez-Zahraouy, M. Hamedoun, M. Benaissa, A. Kara, A. Ennaoui and A. Benyoussef. Band-gap engineering of SnO_2. Solar Energy Materials and Solar Cells, vol. 148, pp. 34-38, 2016.
4. B. O'Regan and M. Gratzel. A low-cost, high-efficiency solar cell based on Dye sensitized colloidal TiO_2 films. Nature, vol. 353, pp. 737-740, 1991.
5. S. R. Pendlebury. Charge Carrier Dynamics in Hematite Photoanodes for Solar Water Oxidation, PhD Thesis, Imperial College London, pp. 1-135, 2012.
6. S. N. Karthick, K. V. Hemalatha, S. K. Balasingam, F. Manik Clinton, S. Akshaya, and H. J. Kim. Dye-sensitized solar cells: History, components, configuration, and working principle. Interfacial Engineering in Functional Materials for Dye Sensitized Solar Cells, pp. 1-16, 2020.
7. K. Basu, D. Benetti, H. Zhao, L. Jin, F. Vetrone, A. Vetrone and F. Rosei. Enhanced photovoltaic properties in dye sensitized solar cells by surface treatment of SnO_2 photoanodes. Scientific reports, vol. 6, no. 1, pp. 23312, 2016.
8. S. E. Lachhab, A. Bliya, H. Diyagh, H. En-nkhili, H. Shindou, S. Ouhassain, H. Slimane, E. Ibrahim and L. Dlimi. Comparative evaluation of SnO_2/CdS/$CuBi_2O_4$ structure performance based on SnO_2 window layer numerical and experimental analysis. Journal of the Indian Chemical Society, vol. 99, no. 10, pp. 100699, 2022.
9. M. Ali, O. Qreshah, A. Ismail, F. Harraz, H. Algami, M. Faisal and W. Chiu. Morphological and optical properties of SnO_2 doped ZnO nanocomposites for electrochemical sensing of hydrazine. International Journal of Electrochemical Science, vol. 14, no. 2, pp. 1461-1478, 2019.
10. P. S. Kolhe , P. M. Koinkar, N. Maiti and K. M. Sonawane: Synthesis of Ag doped SnO_2 thin films for the evaluation of H_2S gas sensing properties. Physical B Condensed Matter, vol. 524, no. 6, pp. 90-96, 2017.

11. P. N. Samanta, D. Majumdar, S. Roszak and J. Leszczynski. First-Principles Approach for Assessing Cold Electron Injection Efficiency of Dye-Sensitized Solar Cell: Elucidation of Mechanism of Charge Injection and Recombination. Journal of Physical Chemistry C, vol. 124, no. 5, pp. 2817-2836, 2020.
12. M. A. K. L. Dissanayake, K. Umair, G. K. R. Senadeera, J. Jaseetharan, T. Weerasinghe and H. W. M. A. C. Wijayasinghe. Plasmonic gold nanoparticle incorporated MgO-coated SnO_2 photoanode for efficiency enhancement in dye sensitized solar. Solar Energy, vol. 161, no 3, pp. 363-377, 2022.
13. P. N. Samanta, D. Majumdar, S. Roszak and J. Leszczynski. First-Principles Approach for Assessing Cold Electron Injection Efficiency of Dye-Sensitized Solar Cell: Elucidation of Mechanism of Charge Injection and Recombination. Journal of Physical Chemistry C, vol. 124, no. 5, pp. 2817–2836, 2020.
14. H. Ohno, S. Nohara, K. Kakinuma, M. Uchida and H. Uchida. Effect of Electronic Conductivities of Iridium Oxide/Doped SnO_2 Oxygen-Evolving Catalysts on the Polarization Properties in Proton Exchange Membrane Water Electrolysis. Catalysts, vol. 9, no. 1, pp. 74, 2019.
15. H. Pan, X. Meng, J. Cai, S. Li and G. Qin. 4d transition-metal doped hematite for enhancing photoelectrochemical activity: Theoretical prediction and experimental confirmation. Royal Society of Chemistry Advances, vol. 5, no. 25, pp. 19353-19361, 2015.
16. V. H. Tran, S. H. Edom, S. C. Yoon, S. K. Kim and S. H. Lee. Enhancing device performance of inverted organic solar cells with SnO_2/Cs_2CO_3 as dual electron transport layers. Organic Electronics: physics, materials, applications, vol. 68, no. 2, pp. 85-95, 2019.
17. J. Bisquert. Theory of the impedance of electron diffusion and recombination in a thin layer. Journal of Physical Chemistry B, vol. 106, no. 2, pp. 325-333, 2002.
18. T. Ma , L. Sun, Q. Niu, Y. Xu, K. Zhu ,X. Liu, X. Guo, and J. Zhang. N-doped carbon-coated Tin sulfide/graphene nanocomposite for enhanced lithium storage. Electrochem Acta, vol. 300, pp. 131-13, 2019.
19. Z. Q. Li, Y. L. Yin, X. D. Liu, L. Y. Li, H. Liu and Q. G. Song. Electronic structure and optical properties of Sb-doped SnO_2. Journal of Applied Physics, vol. 106, no. 8, 2009.

20. S. Pazouki and N. Memarian. Effects of Hydrothermal temperature on the physical properties and anomalous band gap behaviour of ultrafine SnO_2 nanoparticles. Optics, vol. 246, pp. 167843, 2021.
21. Z. Lin, N. Li, Z. Chen and P. Fu. The effect of Ni doping concentration on the gas sensing properties of Ni doped SnO_2. Sensors and Actuators B Chemistry, vol. 239, pp. 501- 510, 2017.
22. W. Zhou, Y. Liu and Y. Yang. The effect of miss-match strain on the structural electronic and optical properties in SnO_2 epitaxial thin films systematically investigating using experimental and theorical methods, Journal of Chemical Physics, vol. 12, no. 118, pp. 6448-6453, 2014.
23. J. C. Ho, R. Yerushalmi, G. Smith, P. Majhi, J. Bennett, J. Halim, N. V. Faifer and A. Javey, Wafer-scale, sub-5 nm junction formation by monolayer doping and conventional spike annealing. Nano Letters, vol. 9, no. 2, pp. 725-730, 2009.
24. Y. H. Liang and E. Tower, Progress in efficient doping of high Aluminium-containing group III-nitrides. Applied Physics Reviews, vol. 5 no 1, 2018.
25. B. Lüssem, M. Riede and K Leo, Doping of organic semiconductors. physica status solidi, vol. 210, no. 1, pp. 9-43, 2013.
26. N. Afify, G. Abbady, D. Hamad, R. F. Abdelbaki, E. R. Shaaban and S. M. N. Abdel, The effective role of dilute Co on SnO_2 nanoparticles: Structural, optical and magnetic characterization properties for spintronics. Sensors and Actuators A: Physical, vol. 331, pp. 112984, 2021.
27. M. Anas, A. Ali, A. G. Khan, A. Alhodaib, A. Zaman, T. Ahmad, V. Tirth, A. Algahtani, S. Ahmad, B.S Abdullaeva and T. Al-Mughanam, Influence of Zirconium (Zr^{4+}) Substitution on the Crystal Structure and Optical and Dielectric Properties of $Sr_{0.8}Mg_{0.2}(Sn_{1-x}Zr_x)O_3$ Ceramics. ACS omega, vol. 8, no. 37, pp. 33794-33801, 2023.
28. S. N. Sarangi, G. K. Pradhan and D. Samal, Band gap engineering in SnO_2 by Pb doping. Journal of Alloys and Compounds, vol. 762, pp. 16-20, 2018.
29. P. P. Filippatos, N. Kelaidis, M. Vasilopoulou, D. Davazoglou and A. Chroneos, Defect processes in halogen doped SnO_2. Applied Sciences, vol. 11, no. 2, pp. 551. 2021.
30. M. Oshima and K. Yoshino, Structural and electronic structure of SnO_2 by the first-principle study. Materials Science Forum vol. 725, pp. 265-268, 2012.

31. G. Bhatia, A. D. Acharya, M. M. Patidar, V. K. Gupta, S. B. Shrivastava and V. Ganesan, Tuning of structural, morphological, optical, and electrical properties of SnO_2 by indium inclusion. Bulletin of Materials Science, vol. 44, no. 3, pp. 187, 2021.
32. T. Duan, Q. Wen, Y. Chen, Y. Zhou and Y. Duan, Enhancing electrocatalytic performance of Sb-doped SnO_2 electrode by compositing nitrogen-doped graphene nanosheets. Journal of hazardous materials, vol. 280, pp. 304-314, 2014.
33. P. P. Filippatos, N. Kelaidis, M. Vasilopoulou, D. Davazoglou and A. Chroneos, Impact of boron and indium doping on the structural, electronic and optical properties of SnO_2. Scientific Reports, vol. 11, no. 1, pp. 13031, 2021.
34. W. Zhang, K. Wang, L. Fan, L. Liu, P. Guo, C. Zou, J. Wang, H. Qian, K. Ibrahim, W. Yan, and F. Xu, Hole carriers doping effect on the metal–insulator transition of N-incorporated vanadium dioxide thin films. The Journal of Physical Chemistry C, vol. 118, no. 24, pp. 12837-12844, 2014.
35. Z. M. Jarzebski and J. P. Marton, Physical properties of SnO_2 materials: I. preparation and defect structure. Journal of the electrochemical Society, vol. 123, no. 7, pp. 199C, 1976.
36. G. K. Deyu, D. Muñoz-Rojas, L. Rapenne, J. L. Deschanvres, A. Klein, C. Jiménez and D. Bellet, SnO_2 films deposited by ultrasonic spray pyrolysis: influence of al incorporation on the properties. Molecules, vol. 24, no. 15, pp. 2797, 2019.
37. R. Ramarajan, M. Kovendhan, K. Thangaraju and D. P. Joseph, Substrate temperature dependent physical properties of spray deposited antimony-doped SnO_2 thin films. Thin Solid Films, vol. 704, pp. 137988, 2020.
38. Z. Gu, P. Liang, and W. Zhang, Sol-gel derived Sb-doped SnO_2/SiO_2 Nano-composite thin films for gas sensors. In Micro-and Nanoelectronics, vol. 6260, pp. 142-149, 2006.
39. H. Zhang, J. Qian, J. Zhang and J. Xu, Enhancing the electrochemical activity and stability of Sb-SnO_2 based electrodes by the introduction of nickel oxide. Journal of Alloys and Compounds, vol. 882, pp. 160700, 2021.
40. J. J. Goings, P. J. Lestrange and X. Li. Real-time time-dependent electronic structure theory. Wiley Interdisciplinary Reviews: Computational Molecular Science, vol. 8, no. 1, pp. 1-19, 2018.

41. S. K. Ghosh, M. Berkowitz and R. G. Parr. Transcription of ground-state density functional theory into local thermodynamics. Proceedings of the National Academy of Sciences of the United States of America, vol. 81, no. 24, pp. 8028-8031, 1984.
42. M. D. Segall, P. Lindan, M. Probert, C. Pickard, P. Hasani, S. Clark and M. Payne. First principles simulation: Ideas, illustrations and the CASTEP code. Journal of Physics Condensed Matter, vol. 14, no. 11, pp. 2717-2744, 2002.
43. M. D. Feit, J. A. Fleck and A. Steiger. Solution of the Schrödinger equation by a spectral method. Journal of Compute Physics, vol. 47, no. 3, pp. 412-433, 1982.
44. D. Becke. Density-functional exchange-energy approximation with correct asymptotic behaviour. Physical Review, vol. 38, no. 6. pp. 3098-3100, 1988.
45. J. P. Perdew, M. Erzernhof and K. Burke. Rationale for mixing exact exchange with density functional approximations. The journal of chemistry and physics, vol. 105, no. 22, pp. 9982-9985, 1996.
46. W. Kohn and L. J. Sham. Self-consistent equations including exchange and correlation effects. Physical review, vol. 140, no. 4A, pp. A1133, 1965.
47. L. Liu, J. Zhang, H. Gao, L. Wang, X Jiang and J. Zhao. Tailoring physical properties of graphene: Effects of hydrogenation, oxidation, and grain boundaries by atomistic simulations. Computational Materials Science, vol. 112, pp. 527-546, 2016.
48. A. Togo, F. Oba, I. Tanaka and K. Tatsumi. First-principles calculations of native defects in tin monoxide. Physical Review B, vol. 74, no. 19, pp. 195128, 2006.
49. M. Colic, G. V. Franks, M. L. Fisher and F. F. Lange. Effect of counterion size on short range repulsive forces at high ionic strengths. Langmuir, vol. 13, no. 12, pp. 3129-3135, 1997.
50. W. Li. Influence of electronic structures of doped TiO_2 on their photocatalysis. physica status solidi (RRL)–Rapid Research Letters, vol. 9, no. 1, pp. 10-27, 2015.
51. Y. Marcus. Ionic radii in aqueous solutions. Chemical Reviews, vol. 88, no. 8, pp.1475-1498, 1988.
52. A. Schleife, J. B. Varley, F. Fuchs, C. Rödl, F. Bechstedt, P. Rinke, A Janotti, and C.G. Van de Walle. Tin dioxide from first principles: Quasiparticle electronic states and optical properties. Physical Review B, vol. 83, no. 3, p. 035116, 2011.

53. Z. Luo, S. Lim, Z. Tian, J. Shang, L. Lai, B. MacDonald, C. Fu, Z Shen, T. Yu and J Lin. Pyridinic N doped graphene: synthesis, electronic structure, and electrocatalytic property. Journal of Materials Chemistry, vol. 21, no. 22, pp. 8038-8044, 2011.
54. M. A. Shandiz. Monte Carlo and Density Functional Theory Simulation of Electron Energy Loss Spectra. McGill University (Canada), 2014.
55. R. S. Dima, L. Phuthu, N. E. Maluta, J. K. Kirui and R. R. Maphanga. Electronic, structural, and optical properties of mono-doped and Co-Doped (210) TiO_2 brookite surfaces for application in dye-sensitized solar cells a first principles study. Materials, vol. 14, no. 14, pp. 3918, 2021.
56. Y. Yang, S. Niu, D. Han, T. Liu, G. Wang and Y Li. Progress in developing metal oxide nanomaterials for photoelectrochemical water splitting. Advanced Energy Materials, vol. 7, no. 19, pp. 1700555, 2017.
57. Y. Ma, F. Le Formal, A. Kafizas, S. R. Pendlebury and J. R. Durrant. Efficient suppression of back electron/hole recombination in cobalt phosphate surface-modified undoped bismuth vanadate photoanodes. Journal of materials chemistry A, vol. 3. no. 41, pp. 20649-20657, 2015.
58. A. Ammari, M. Trari, B. Bellal and N. Zebbar. Effect of Sb doping on the transport and electrochemical properties of partially amorphous SnO_2 thin films. Journal of Electroanalytical Chemistry, vol. 823, no. 2, pp. 638-646, 2018.
59. T. M. Pan, B. J. Peng and C. H. Chen. Structural and electrical properties of high $CeTi_xO_y$, $ErTi_xO_y$and $YbTi_xO_y$ gate dielectrics for In-Zn-SnO thin film transistors. Journal of Alloys Compound, vol. 722, pp. 637-643, 2017.
60. F. M. Hossain, A. V. Evteev, I. V. Belova, J. Nowotny and G. E. Murch. First principles calculations of a corrugated anatase TiO_2 surface. Computational Material Sciences, vol. 51, no. 1, pp. 78-82, 2012.